Report from Working Group 2: Higgs physics at the HL-LHC and HE-LHC

Physics of the HL-LHC, and Perspectives at the HE-LHC

Conveners:
M. Cepeda[1,2], *S. Gori*[3], *P. Ilten*[4], *M. Kado*[5,6,7], *F. Riva*[8]

Contributors:
R. Abdul Khalek[9,10], *A. Aboubrahim*[11], *J. Alimena*[12], *S. Alioli*[13,13], *A. Alves*[14], *C. Asawatangtrakuldee*[15], *A. Azatov*[16,17], *P. Azzi*[18], *S. Bailey*[19], *S. Banerjee*[20], *E.L. Barberio*[21], *D. Barducci*[16], *G. Barone*[22], *M. Bauer*[20], *C. Bautista*[23], *P. Bechtle*[24], *K. Becker*[25], *A. Benaglia*[26], *M. Bengala*[27], *N. Berger*[28], *C. Bertella*[29], *A. Bethani*[30], *A. Betti*[24], *A. Biekotter*[31], *F. Bishara*[15], *D. Bloch*[32], *P. Bokan*[33], *O. Bondu*[34], *M. Bonvini*[6], *L. Borgonovi*[35,36], *M. Borsato*[37], *S. Boselli*[38], *S. Braibant-Giacomelli*[35,36], *G. Buchalla*[39], *L. Cadamuro*[40], *C. Caillol*[41], *A. Calandri*[42,43], *A. Calderon Tazon*[44], *J.M. Campbell*[45], *F. Caola*[20], *M. Capozi*[46], *M. Carena*[45,47], *C.M. Carloni Calame*[48], *A. Carmona*[49], *E. Carquin*[50], *A. Carvalho Antunes De Oliveira*[51], *A. Castaneda Hernandez*[52], *O. Cata*[53], *A. Celis*[54], *A. Cerri*[55], *F. Cerutti*[56,57], *G.S. Chahal*[58,20], *A. Chakraborty*[59], *G. Chaudhary*[60], *X. Chen*[61], *A.S. Chisholm*[1,4], *R. Contino*[62], *A.J. Costa*[27], *R. Covarelli*[63,64], *N. Craig*[65], *D. Curtin*[66], *L. D'Eramo*[67], *N.P. Dang*[68], *P. Das*[69], *S. Dawson*[22], *O.A. De Aguiar Francisco*[1], *J. de Blas*[70,18], *S. De Curtis*[71], *N. De Filippis*[72,73], *H. De la Torre*[74], *L. de Lima*[75], *A. De Wit*[15], *C. Delaere*[34], *M. Delcourt*[34], *M. Delmastro*[28], *S. Demers*[76], *N. Dev*[77], *R. Di Nardo*[78], *S. Di Vita*[79], *S. Dildick*[80], *L.A.F. do Prado*[81,23], *M. Donadelli*[82], *D. Du*[83], *G. Durieux*[84,15], *M. Dührssen*[1], *O. Eberhardt*[85], *K. El Morabit*[86], *J. Elias-Miro*[1], *J. Ellis*[87,51,1], *C. Englert*[88], *R. Essig*[89], *S. Falke*[28], *M. Farina*[89], *A. Ferrari*[90], *A. Ferroglia*[91], *M.C.N. Fiolhais*[92], *M. Flechl*[93], *S. Folgueras*[94], *E. Fontanesi*[35,36], *P. Francavilla*[67,95], *R. Franceschini*[96,97], *R. Frederix*[98], *S. Frixione*[99], *G. Gómez-Ceballos*[100], *A. Gabrielli*[56,57], *S. Gadatsch*[1], *M. Gallinaro*[27], *A. Gandrakota*[101], *J. Gao*[102], *F.M. Garay Walls*[103], *T. Gehrmann*[61], *Y. Gershtein*[101], *T. Ghosh*[104], *A. Gilbert*[1], *R. Glein*[105], *E.W.N. Glover*[20], *R. Gomez-Ambrosio*[20], *R. Gonçalo*[27], *D. Gonçalves*[106], *M. Gorbahn*[107], *E. Gouveia*[27], *M. Gouzevitch*[108], *P. Govoni*[26,13], *M. Grazzini*[61], *B. Greenberg*[101], *K. Grimm*[109], *A.V. Gritsan*[110], *A. Grohsjean*[15], *C. Grojean*[15], *J. Gu*[111], *R. Gugel*[25], *R.S. Gupta*[20], *C.B. Gwilliam*[112], *S. Höche*[113], *M. Haacke*[103], *Y. Haddad*[58], *U. Haisch*[46], *G.N. Hamity*[114], *T. Han*[106], *L.A. Harland-Lang*[19], *R. Harnik*[45], *S. Heinemeyer*[44,115], *G. Heinrich*[46], *B. Henning*[8], *V. Hirschi*[43], *K. Hoepfner*[116], *J.M. Hogan*[117,118], *S. Homiller*[119,22], *Y. Huang*[120], *A. Huss*[1], *S. Jézéquel*[28], *Sa. Jain*[69], *S.P. Jones*[1], *K. Köneke*[25], *J. Kalinowski*[121], *J.F. Kamenik*[122,123], *M. Kaplan*[100], *A. Karlberg*[61], *M. Kaur*[60], *P. Keicher*[86], *M. Kerner*[61], *A. Khanov*[124], *J. Kieseler*[1], *J.H. Kim*[125], *M. Kim*[126], *T. Klijnsma*[43], *F. Kling*[127], *M. Klute*[100], *J.R. Komaragiri*[128], *K. Kong*[125], *J. Kozaczuk*[129], *P Kozow*[121], *C. Krause*[45], *S. Lai*[33], *J. Langford*[58], *B. Le*[21], *L. Lechner*[93], *W.A. Leight*[130], *K.J.C. Leney*[131], *T. Lenz*[24], *C-Q. Li*[132], *H. Li*[83], *Q. Li*[133], *S. Liebler*[134], *J. Lindert*[20], *D. Liu*[135], *J. Liu*[136], *Y. Liu*[137], *Z. Liu*[138,45], *D. Lombardo*[8], *A. Long*[139], *K. Long*[41], *I. Low*[140,135], *G. Luisoni*[46], *L.L. Ma*[83], *A.-M. Magnan*[58], *D. Majumder*[125], *A. Malinauskas*[19], *F. Maltoni*[141], *M.L. Mangano*[1], *G. Marchiori*[67,67], *A.C. Marini*[100], *A. Martin*[77], *S. Marzani*[142,99], *A. Massironi*[1], *K.T. Matchev*[40,143], *R.D. Matheus*[23], *K. Mazumdar*[69], *J. Mazzitelli*[61], *A.E. Mcdougall*[21], *P. Meade*[119], *P. Meridiani*[6], *A.B. Meyer*[15], *E. Michielin*[18], *P. Milenovic*[1,144], *V. Milosevic*[58], *K. Mimasu*[141], *B. Mistlberger*[145], *M. Mlynarikova*[146], *M. Mondragon*[147], *P.F. Monni*[1], *G. Montagna*[148,48], *F. Monti*[26,13], *M. Moreno Llacer*[1], *A. Mueck*[149], *P.C. Muiño*[27], *C. Murphy*[150], *W.J. Murray*[151], *P. Musella*[43], *M. Narain*[118], *R.F. Naranjo Garcia*[130], *P. Nath*[11], *M. Neubert*[152], *O. Nicrosini*[48], *K. Nikolopoulos*[4], *A. Nisati*[6,7], *J.M. No*[115], *M.L. Ojeda*[153], *S.A. Olivares Pino*[103], *A. Onofre*[154], *G. Ortona*[155], *S. Pagan Griso*[56,57], *D. Pagani*[98], *E. Palencia Cortezon*[94], *C. Palmer*[156], *C. Pandini*[1], *G. Panico*[157,71], *L. Panwar*[128], *D. Pappadopulo*[158], *M. Park*[159], *R. Patel*[105], *F. Paucar-Velasquez*[101], *K. Pedro*[45], *L. Pernie*[80], *L. Perrozzi*[43], *B.A. Petersen*[1], *E. Petit*[160], *G. Petrucciani*[1], *G. Piacquadio*[161], *F. Piccinini*[48], *M. Pieri*[162], *T. Plehn*[37], *S. Pokorski*[121], *A. Pomarol*[163],

https://doi.org/10.23731/CYRM-2019-007.221

E. Ponton[23,164], *S. Pozzorini*[61], *S. Prestel*[45], *K. Prokofiev*[165], *M. Ramsey-Musolf*[166], *E. Re*[1,167], *N.P. Readioff*[160], *D. Redigolo*[168,169], *L. Reina*[170], *E. Reynolds*[4,4], *M. Riembau*[8], *F. Rikkert*[98], *T. Robens*[171], *R. Roentsch*[172,1], *J. Rojo*[10], *N. Rompotis*[112], *J. Rorie*[139], *J. Rosiek*[121], *J. Roskes*[110], *J.T. Ruderman*[158], *N. Sahoo*[69], *S. Saito*[69], *R. Salerno*[155], *P.H. Sales De Bruin*[173], *A. Salvucci*[174], *K. Sandeep*[60], *J. Santiago*[175], *R. Santo*[27], *V. Sanz*[55], *U. Sarica*[110], *A. Savin*[41], *A. Savoy-Navarro*[81,176], *S. Sawant*[69], *A.C. Schaffer*[5], *M. Schlaffer*[177], *A. Schmidt*[116], *B. Schneider*[45], *R. Schoefbeck*[93], *M. Schröder*[86], *M. Scodeggio*[130], *E. Scott*[58], *L. Scyboz*[46], *M. Selvaggi*[1], *L. Sestini*[18], *H.-S. Shao*[178], *A. Shivaji*[141,179], *L. Silvestrini*[6,1], *L. Simon*[149], *K. Sinha*[180], *Y. Soreq*[1,84], *M. Spannowsky*[181], *M. Spira*[182], *D. Spitzbart*[93], *E. Stamou*[47], *J. Stark*[160], *T. Stefaniak*[15], *B. Stieger*[183,184], *G. Strong*[27], *M. Szleper*[185], *K. Tackmann*[130], *M. Takeuchi*[186], *S. Taroni*[77], *M. Testa*[187], *A. Thamm*[1], *V. Theeuwes*[188,189], *L.A. Thomsen*[76], *S. Tkaczyk*[45], *R. Torre*[99,1], *F. Tramontano*[190,191], *K.A. Ulmer*[105], *T. Vantalon*[15], *L. Vecchi*[192], *R. Vega-Morales*[175], *E. Venturini*[16], *M. Verducci*[97,96], *C. Vernieri*[113], *T. Vickey*[114], *M. Vidal Marono*[34], *P. Vischia*[94], *E. Vryonidou*[1], *P. Wagner*[24], *V.M. Walbrecht*[46], *L.-T. Wang*[136], *N. Wardle*[58], *D.R. Wardrope*[193], *G. Weiglein*[15], *S. Wertz*[34], *M. Wielers*[194], *J.M. Williams*[100], *R. Wolf*[86], *A. Wulzer*[1], *M. Xiao*[110], *H.T. Yang*[56,57], *E. Yazgan*[120], *Z. Yin*, *T. You*[195,38], *F. Yu*[49,196], *G. Zanderighi*[1,46], *D. Zanzi*[1], *M. Zaro*[10,10], *S.C. Zenz*[58,197], *D. Zerwas*[5], *M. Zgubič*[198], *J. Zhang*[83], *L. Zhang*[137], *W. Zhang*[118], *X. Zhao*[34,22], *Y.-M. Zhong*[199]

[1]CERN, Geneva; [2]CIEMAT, Madrid; [3]UC, Santa Cruz, SCIPP; [4]U. Birmingham, Sch. Phys. Astron.; [5]LAL, Orsay; [6]INFN, Rome 1; [7]U. Rome 1, La Sapienza, Dept. Phys.; [8]U. Geneva, Dept. Theor. Phys.; [9]Vrije U., Amsterdam, Dept. Phys. Astron.; [10]Nikhef, Amsterdam; [11]Northeastern U.; [12]Ohio State U., Columbus; [13]U. Milan Bicocca, Dept. Phys.; [14]Diadema, Sao Paulo Fed. U.; [15]DESY, Hamburg; [16]SISSA, Trieste; [17]INFN, Trieste; [18]INFN, Padua; [19]U. Oxford, Ctr. Theor. Phys.; [20]Durham U., IPPP; [21]ARC, CoEPP, Melbourne; [22]Brookhaven Natl. Lab., Dept. Phys.; [23]UNESP Sao Paulo, IFT; [24]U. Bonn, Phys. Inst.; [25]U. Freiburg, Inst. Phys.; [26]INFN, Milan Bicocca; [27]LIP, Lisbon; [28]LAPP, Annecy; [29]CAS, Beijing; [30]U. Manchester, Sch. Phys. Astron.; [31]U. Heidelberg, ITP; [32]IPHC, Strasbourg; [33]U. Gottingen, II. Phys. Inst.; [34]Cathol. U. Louvain, CP3; [35]INFN, Bologna; [36]U. Bologna, Dept. Phys.; [37]U. Heidelberg, Phys.Inst.; [38]U. Cambridge; [39]LMU Munich; [40]U. Florida, Gainesville, Dept. Phys.; [41]U. Wisconsin, Madison, Dept. Phys.; [42]CPPM, Marseille; [43]ETH, Zurich, Dept. Phys.; [44]IFCA, Santander; [45]Fermilab; [46]MPI Phys., Munich; [47]U. Chicago; [48]INFN, Pavia; [49]U. Mainz, PRISMA; [50]U. Tech. Federico Santa Maria, Valparaiso; [51]NICPB, Tallinn; [52]Sonora U.; [53]U. Siegen, Dept. Phys.; [54]LMU Munich, Dept. Phys.; [55]U. Sussex, Brighton, Dept. Phys. Astron.; [56]LBNL, Berkeley, Div. Phys.; [57]UC, Berkeley, Dept. Phys.; [58]Imperial Coll., London, Dept. Phys.; [59]KEK, Tsukuba; [60]Panjab U., Chandigarh; [61]U. Zurich, Phys. Inst.; [62]Scuola Normale Superiore, Pisa; [63]INFN, Turin; [64]U. Turin, Dept. Exp. Phys.; [65]UC, Santa Barbara, Dept. Phys.; [66]U. Toronto; [67]LPNHE, Paris; [68]U. Louisville, Dept. Phys.; [69]TIFR, Mumbai, DHEP; [70]U. Padua, Dept. Phys.; [71]INFN, Florence; [72]INFN, Bari; [73]Polytech. Bari; [74]Michigan State U., East Lansing, Dept. Phys. Astron.; [75]Federal da Fronteira Sul U.; [76]Yale U., Dept. Phys.; [77]U. Notre Dame, Dept. Phys.; [78]UMass, Amherst, Dept. Phys.; [79]INFN, Italy; [80]TAMU, College Station; [81]IRFU, Saclay, DPP; [82]U. Sao Paulo, Inst. Phys.; [83]Shandong U., Jinan; [84]Technion, IIT, Dept. Phys.; [85]IFIC, Valencia; [86]KIT, Karlsruhe, ETP; [87]King's Coll. London; [88]U. Glasgow, Sch. Phys. Astron.; [89]Stony Brook U.; [90]Uppsala U., Dept. Phys. Astron.; [91]CUNY, City Tech.; [92]CUNY, BMCC; [93]OEAW, Vienna; [94]U. Oviedo, Dept. Phys.; [95]INFN, Pisa; [96]U. Rome 3, Dept. Math. Phys.; [97]INFN, Rome 3; [98]Tech. U., Munich, Dept. Phys.; [99]INFN, Genoa; [100]MIT, Cambridge; [101]Rutgers U., Piscataway, Dept. Phys. Astron.; [102]SJTU, Sch. Phys. Astron., Shanghai; [103]Pontificia U. Catol. Chile, Santiago, Dept. Phys.; [104]U. Hawaii; [105]U. Colorado, Boulder, Dept. Phys.; [106]U. Pittsburgh; [107]U. Liverpool; [108]IPNL, Lyon; [109]Cal State, East Bay; [110]Johns Hopkins U.; [111]UC, Davis; [112]U. Liverpool, Dept. Phys.; [113]SLAC; [114]U. Sheffield, Dept. Phys. Astron.; [115]IFT, Madrid; [116]RWTH Aachen; [117]Bethel Coll.; [118]Brown U., Dept. Phys.; [119]Stony Brook U., YITP; [120]CAS, IHEP, Beijing; [121]U. Warsaw, Fac. Phys.; [122]J. Stefan Inst., Ljubljana; [123]U. Ljubljana, Fac. Math. Phys.; [124]OKState, Stillwater, Dept. Phys.; [125]U. Kansas, Lawrence, Dept. Phys. Astron.; [126]POSTECH, Pohang; [127]UC, Irvine, Dept. Phys. Astron.; [128]Indian Inst. Sci., Bangalore; [129]U. Illinois, Urbana-Champaign; [130]DESY, Zeuthen;

[131]Southern Methodist U., Dept. Phys.; [132]USTC, Hefei, DMP; [133]Peking U., Beijing, Sch. Phys.; [134]KIT, Karlsruhe, TP; [135]Argonne Natl. Lab., HEP Div.; [136]Chicago U., EFI; [137]Nanjing U., Dept. Phys.; [138]U. Maryland, College Park, Dept. Phys.; [139]Rice U., Dept. Phys. Astron.; [140]Northwestern U., Dept. Phys. Astron.; [141]Cathol. U. Louvain; [142]U. Genoa, Dept. Phys.; [143]U. Florida, Gainesville; [144]U. Belgrade; [145]MIT, Cambridge, CTP; [146]Charles U., Prague, Inst. Part. Nucl. Phys.; [147]UNAM, Mexico, IFUNAM; [148]U. Pavia, Dept. Nucl. Theor. Phys.; [149]RWTH, Aachen, Phys. Inst.; [150]Brookhaven Natl. Lab.; [151]U. Warwick, Dept. Phys.; [152]U. Mainz; [153]U. Toronto, Dept. Phys.; [154]U. Minho, Dept. Math.; [155]LLR, Palaiseau; [156]Princeton U.; [157]U. Florence, Dept. Phys. Astron.; [158]New York U.; [159]Seoultech, Seoul; [160]LPSC, Grenoble; [161]Stony Brook U., Dept. Phys. Astron.; [162]UC, San Diego, Dept. Phys.; [163]U. Barcelona, IFAE; [164]ICTP-SAIFR, Sao Paulo; [165]HKUST, Hong Kong; [166]UMass, Amherst; [167]LAPTH, Annecy; [168]Tel-Aviv U., Dept. Part. Phys.; [169]IAS, Princeton; [170]Florida State U., Tallahassee, Dept. Phys.; [171]RBT, Zagreb; [172]KIT, Karlsruhe, Dept. Phys.; [173]U. Washington, Seattle, Dept. Phys.; [174]Chinese U. Hong Kong; [175]U. Granada, CAFPE; [176]APC, Paris; [177]Weizmann Inst. Sci., Rehovot, Fac. Phys.; [178]LPTHE, Paris; [179]IISER, Mohali; [180]U. Oklahoma, Norman; [181]Durham U., Dept. Phys.; [182]PSI, Villigen; [183]U. Nebraska, Lincoln; [184]U. Nebraska, Lincoln, Dept. Phys. Astron.; [185]NCBJ, Warsaw; [186]U. Tokyo; [187]INFN, LNF, Frascati; [188]U. Gottingen, Inst. Theor. Phys.; [189]IPhT, Saclay; [190]U. Naples, Dept. Phys. Sci.; [191]INFN, Naples; [192]EPFL, Lausanne, LPTP; [193]U. Coll. London, Dept. Phys. Astron.; [194]RAL, Didcot; [195]U. Cambridge, Cavendish Lab.; [196]U. Mainz, Inst. Phys.; [197]Queen Mary U. London, Sch. Phys. Astron.; [198]U. Oxford, Part. Phys. Dept.; [199]Boston U.

Abstract

The discovery of the Higgs boson in 2012, by the ATLAS and CMS experiments, was a success achieved with only a percent of the entire dataset foreseen for the LHC. It opened a landscape of possibilities in the study of Higgs boson properties, Electroweak Symmetry breaking and the Standard Model in general, as well as new avenues in probing new physics beyond the Standard Model. Six years after the discovery, with a conspicuously larger dataset collected during LHC Run 2 at a 13 TeV centre-of-mass energy, the theory and experimental particle physics communities have started a meticulous exploration of the potential for precision measurements of its properties. This includes studies of Higgs boson production and decays processes, the search for rare decays and production modes, high energy observables, and searches for an extended electroweak symmetry breaking sector. This report summarises the potential reach and opportunities in Higgs physics during the High Luminosity phase of the LHC, with an expected dataset of pp collisions at 14 TeV, corresponding to an integrated luminosity of 3 ab^{-1}. These studies are performed in light of the most recent analyses from LHC collaborations and the latest theoretical developments. The potential of an LHC upgrade, colliding protons at a centre-of-mass energy of 27 TeV and producing a dataset corresponding to an integrated luminosity of 15 ab^{-1}, is also discussed.

Contents

1 Introduction

One of the main goals of the physics program at the Large Hadron Collider is to elucidate the origin of electroweak symmetry breaking.

Relativistic quantum field and gauge theories have been remarkably successful to describe fundamental particles and their interactions. In this context, the seminal work of Brout, Englert [1], Higgs [2, 3, 4] and Guralnik, Hagen and Kibble [5, 6], has provided a consistent mechanism for the generation of gauge boson masses. The Glashow-Weinberg-Salam theory extended this mechanism proposing a theory of the electroweak interactions [7, 8, 9], introducing a doublet of complex scalar fields, which couples also to fermions, providing them with a mass which would otherwise be absent. This is now known as the Standard Model (SM) of particle physics. A complete and detailed description of the Higgs mechanism can be found at [10]. A salient prediction of the theory is the presence of a Higgs boson. The discovery of the Higgs boson with a mass of 125 GeV, during the first run of the LHC at reduced centre-of-mass energies of 7 TeV and 8 TeV, is a landmark result that has reshaped the landscape of High Energy physics [11, 12]. The mass of the Higgs boson is particularly favourable as it allows to measure directly a large number of its couplings. It has also important consequences in terms of probing the self-consistency of the Standard Model both through the global fit of precision observables and through its interpretation as a measure of the Higgs boson self coupling, allowing to extrapolate the SM at higher energies and verify the stability of the vacuum.

The existence of the Higgs boson as a light scalar leads to the hierarchy or naturalness problem, as its mass at the weak scale happens to be particularly sensitive to general larger scales beyond the SM (BSM), therefore apparently requiring a large fine tuning of fundamental parameters. Addressing the naturalness problem is and has been for decades one of the main guiding principles for the development of theories beyond the Standard Model. There are two main classes of theories attempting to address the naturalness problem: the first are weakly coupled theories, where the Higgs boson remains an elementary scalar and its mass is protected by additional symmetries, as in Supersymmetric theories. The second are strongly coupled solutions, which involve new strong interactions at approximately the TeV scale and deliver naturally light composite scalars as Pseudo Nambu-Goldstone bosons. Both approaches can have large effects on the phenomenology of the Higgs particle and in some cases predict new states that could be observed at the LHC.

Other questions of fundamental importance can affect the phenomenology of the Higgs boson. The question of the nature of the Electroweak Phase transition is strongly intertwined with Higgs physics where, in many scenarios, a detailed study of the Higgs pair production can reveal the strength of the transition. Similarly, certain models of Dark Matter involve potentially large effects on the phenomenology of the Higgs particle. These fundamental questions, and many more, can be addressed by the study of the Higgs boson at the LHC and its high luminosity (HL) and high energy (HE) upgrades.

Since the discovery, a large campaign of measurements of the properties of the Higgs boson has started, including exclusive production modes and differential cross sections. Many new ideas have emerged during the completion of this program. This chapter presents a reappraised estimate of the potential of the HL-LHC and the HE-LHC projects to measure the properties of the Higgs boson, highlighting the opportunities for measurements of fundamental importance.

Section 2 presents the foreseen program for precision measurements of the Higgs boson coupling properties through exclusive production modes and differential cross sections. Section 3 presents the potential to measure double Higgs production and to constrain the Higgs trilinear coupling, both through the double Higgs production and indirect probes from single Higgs boson production. Section 4 is devoted to a new class of measurements unique to the HL-HE program: high-energy probes. These include Higgs processes like associated production of a Higgs and a W or Z boson, or vector boson fusion (VBF), for which the centre-of-mass energy is not limited to the Higgs mass, and it extends to Drell Yan, di-boson processes and vector boson scattering, which provide a context in which high-energy

measurements can be associated with precision observables. Section 5 focuses on measurements of the Higgs mass and opportunities for the measurement of the Higgs boson width. Section 6 describes the constraints on the invisible decays of the Higgs boson and the indirect constraints on the couplings of the Higgs boson to undetected particles from the measurement of the Higgs boson couplings, in particular in the framework of Higgs portal and dark matter models. Section 7 will discuss approaches to constrain light and non diagonal Higgs Yukawa couplings directly and indirectly. Section 8 is devoted to a global interpretation of the measurements in the framework of the Standard Model Effective Field Theory. Section 9 is devoted to the discussion of the prospects for probing additional Higgs bosons both with a mass above or below 125 GeV, and for discovering a wide range of exotic Higgs boson decays.

1.1 Experimental analysis methods and objects definitions

Different approaches have been used by the experiments and in theoretical prospect studies, hereafter named projections, to assess the sensitivity in searching for new physics at the HL-LHC and HE-LHC. For some of the projections, a mix of the approaches described below is used, in order to deliver the most realistic result. The total integrated luminosity for the HL-LHC dataset is assumed to be 3000 fb^{-1} at a centre-of-mass energy of 14 TeV. For HE-LHC studies the dataset is assumed to be 15 ab^{-1} at a centre-of-mass of 27 TeV. The effect of systematic uncertainties is taken into account based on the studies performed for the existing analyses and using common guidelines for projecting the expected improvements that are foreseen thanks to the large dataset and upgraded detectors, as described in Section 1.1.3.

Detailed-simulations are used to assess the performance of reconstructed objects in the upgraded detectors and HL-LHC conditions, as described in Sections 1.1.1,1.1.2. For some of the projections, such simulations are directly interfaced to different event generators, parton showering (PS) and hadronisation generators. Monte Carlo (MC) generated events are used for SM and BSM processes, and are employed in the various projections to estimate the expected contributions of each process.

Extrapolations of existing results rely on the existent statistical frameworks to estimate the expected sensitivity for the HL-LHC dataset. The increased centre-of-mass energy and the performance of the upgraded detectors are taken into account for most of the extrapolations using scale factors on the individual processes contributing to the signal regions. Such scale factors are derived from the expected cross sections and from detailed simulation studies.

Fast-simulations are employed for some of the projections in order to produce a large number of Monte Carlo events and estimate their reconstruction efficiency for the upgraded detectors. The upgraded CMS detector performance is taken into account encoding the expected performance of the upgraded detector in DELPHES [13], including the effects of pile-up interactions. Theoretical contributions use DELPHES with the commonly accepted HL-LHC card corresponding to the upgraded ATLAS and CMS detectors.

Parametric-simulations are used for some of the projections to allow a full re-optimisation of the analysis selections that profit from the larger available datasets. Particle-level definitions are used for electrons, photons, muons, taus, jets and missing transverse momentum. These are constructed from stable particles of the MC event record with a lifetime larger than 0.3×10^{-10} s within the observable pseudorapidity range. Jets are reconstructed using the anti-k_t algorithm [14] implemented in the FastJet [15] library, with a radius parameter of 0.4. All stable final-state particles are used to reconstruct the jets, except the neutrinos, leptons and photons associated to W or Z boson or τ lepton decays. The effects of an upgraded ATLAS detector are taken into account by applying energy smearing, efficiencies and fake rates to generator level quantities, following parametrisations based on detector performance studies with the detailed simulations. The effect of the high pileup at the HL-LHC is incorporated by overlaying pileup jets onto the hard-scatter events. Jets from pileup are randomly selected as jets to be considered for analysis with $\sim 2\%$ efficiency, based on studies of pile-up jet rejection and current experience.

1.1.1 ATLAS and CMS performance

The expected performance of the upgraded ATLAS and CMS detectors has been studied in detail in the context of the Technical Design Reports and subsequent studies; the assumptions used for this report and a more detailed description are available in Ref. [16, 17]. For CMS, the object performance in the central region assumes a barrel calorimeter ageing corresponding to an integrated luminosity of 1000 fb^{-1}.

The triggering system for both experiments will be replaced and its impact on the triggering abilities of each experiment assessed; new capabilities will be added, and, despite the more challenging conditions, most of the trigger thresholds for common objects are expected to either remain similar to the current ones or to even decrease [18, 19].

The inner detector is expected to be completely replaced by both experiments, notably extending its coverage to $|\eta| < 4.0$. The performance for reconstructing charged particles has been studied in detail in Ref. [20, 21, 22].

Electrons and photons are reconstructed from energy deposits in the electromagnetic calorimeter and information from the inner tracker [23, 24, 25, 26]. Several identification working points have been studied and are employed by the projection studies as most appropriate.

Muons are reconstructed combining muon spectrometer and inner tracker information [27, 28].

Jets are reconstructed by clustering energy deposits in the electromagnetic and hadronic calorimeters [29, 23, 24] using the anti-k_T algorithm [14]. B-jets are identified via b-tagging algorithms. B-tagging is performed if the jet is within the tracker acceptance ($|\eta| < 4.0$). Multivariate techniques are employed in order to identify $b-$jets and $c-$jets, and were fully re-optimised for the upgraded detectors [20, 22]. An 70% $b-$jet efficiency working point is used, unless otherwise noted.

High p_T boosted jets are reconstructed using large-radius anti-k_T jets with a distance parameter of 0.8. Various jet substructure variables are employed to identify boosted W/Z/Higgs boson and top quark jets with good discrimination against generic QCD jets.

Missing transverse energy is reconstructed following similar algorithms as employed in the current data taking. Its performance has been evaluated for standard processes, such as top pair production [20, 30].

The addition of new precise-timing detectors and its effect on object reconstruction has also been studied in Ref. [31, 26], although its results are only taken into account in a small subset of the projections in this report.

1.1.2 LHCb

The LHCb upgrades are shifted with respect to those of ATLAS and CMS. A first upgrade will happen at the end of Run 2 of the LHC, to run at a luminosity five times larger (2×10^{33}cm^{-2}s^{-1}) in LHC Run 3 compared to those in Runs 1 and 2, while maintaining or improving the current detector performance. This first upgrade phase (named Upgrade I) will be followed by by the so-called Upgrade II phase (planned at the end of Run 4) to run at an even more challenging luminosity of $\sim 2\times10^{34}$cm^{-2}s^{-1}.

The LHCb MC simulation used in this document mainly relies on the PYTHIA 8 generator [32] with a specific LHCb configuration [33], using the CTEQ6 leading-order set of parton density functions [34]. The interaction of the generated particles with the detector, and its response, are implemented using the GEANT toolkit [35, 36], as described in Ref. [37].

The reconstruction of jets is done using a particle flow algorithm, with the output of this clustered using the anti-kT algorithm as implemented in FastJet, with a distance parameter of 0.5. Requirements are placed on the candidate jet in order to reduce the background formed by particles which are either incorrectly reconstructed or produced in additional pp interactions in the same event.

Concerning the increased pile-up, different assumptions are made, but in general the effect is assumed to be similar to the one in Run 2.

1.1.3 Treatment of systematic uncertainties

It is a significant challenge to predict the expected systematic uncertainties of physics results at the end of HL-LHC running. It is reasonable to anticipate improvements to techniques of determining systematic uncertainties over an additional decade of data-taking. To estimate the expected performance, experts in the various physics objects and detector systems from ATLAS and CMS have looked at current limitations to systematic uncertainties in detail to determine which contributions are limited by statistics and where there are more fundamental limitations. Predictions were made taking into account the increased integrated luminosity and expected potential gains in technique. These recommendations were then harmonised between the experiments to take advantage of a wider array of expert opinions and to allow the experiments to make sensitivity predictions on equal footing [16, 17]. For theorists' contributions, a simplified approach is often adopted, loosely inspired by the improvements predicted by experiments.

General guide-lining principles were defined in assessing the expected systematic uncertainties. Theoretical uncertainties are assumed to be reduced by a factor of two with respect to the current knowledge, thanks to both higher-order calculation as well as reduced parton distribution functions (PDF) uncertainties [38]. All the uncertainties related to the limited number of simulated events are neglected, under the assumption that sufficiently large simulation samples will be available by the time the HL-LHC becomes operational. For all scenarios, the intrinsic statistical uncertainty in the measurement is reduced by a factor $1/\sqrt{\mathrm{L}}$, where L is the projection integrated luminosity divided by that of the reference Run 2 analysis. Systematics driven by intrinsic detector limitations are left unchanged, or revised according to detailed simulation studies of the upgraded detector. Uncertainties on methods are kept at the same value as in the latest public results available, assuming that the harsher HL-LHC conditions will be compensated by method improvements.

The uncertainty in the integrated luminosity of the data sample is expected to be reduced down to 1% by a better understanding of the calibration methods and their stability employed in its determination, and making use of the new capabilities of the upgraded detectors.

In addition to the above scenario (often referred to as "YR18 systematics uncertainties" scenario), results are often compared to the case where the current level of understanding of systematic uncertainties is assumed ("Run 2 systematic uncertainties") or to the case of statistical-only uncertainties.

1.2 Implications for beyond the Standard Model theories

1.2.1 Heavy new physics: precision tests and effective field theories

Precision measurements provide an important tool to search for heavy BSM dynamics, associated with mass scales beyond the LHC direct energy reach, exploiting the fact that such dynamics can still have an impact on processes at smaller energy, via virtual effects. In this context the well-established framework of effective field theories (EFTs) allows to systematically parametrise BSM effects and how they modify SM processes. Assuming lepton and baryon number conservation, the leading such effects can be captured by dimension-6 operators,

$$\mathcal{L}_{\text{eff}} = \mathcal{L}_{\text{SM}} + \frac{1}{\Lambda^2}\sum_i c_i \mathcal{O}_i + \cdots \tag{1}$$

for dimensionless coefficients c_i and, for simplicity, a common suppression scale Λ. Table 1 proposes a set of operators considered in this report. This set is *redundant*, in the sense that different combinations of operators might lead to the same physical effect; moreover this set is *not complete*, in the sense that there are more operators at dimension-6 level. In practical applications we will always be interested in identifying *minimal* (non-redundant) subsets of operators that contribute to a given process; we will also be interested that these operators be complete, at least under some well motivated assumption. For instance, the assumption that new physics only couples to the SM bosons, leads to the *universal* set of operators, from the second panel in table 1. Alternatively, the minimal flavour violation assumption [39] provides

a well-motivated framework to focus on operators with a certain, family-universal, flavour structure; operators with a richer flavour structure will be studied in a dedicated section 7.

Table 1: A list of dimension-6 SMEFT operators used in this chapter, defined for one family only; operators suppressed in the minimal flavour violation assumption [39], have been neglected (in particular dipole-type operators). Some combinations are redundant and can be eliminated as described in the text.

Higgs-Only Operators		
$\mathcal{O}_H = \frac{1}{2}(\partial^\mu \lvert H\rvert^2)^2$	$\mathcal{O}_6 = \lambda \lvert H\rvert^6$	
$\mathcal{O}_{y_u} = y_u \lvert H\rvert^2 \bar{Q}\widetilde{H}u$	$\mathcal{O}_{y_d} = y_d \lvert H\rvert^2 \bar{Q}Hd$	$\mathcal{O}_{y_e} = y_e \lvert H\rvert^2 \bar{L}He$
$\mathcal{O}_{BB} = g'^2 \lvert H\rvert^2 B_{\mu\nu}B^{\mu\nu}$	$\mathcal{O}_{GG} = g_s^2 \lvert H\rvert^2 G^A_{\mu\nu}G^{A\mu\nu}$	$\mathcal{O}_{WW} = g^2 \lvert H\rvert^2 W^I_{\mu\nu}W^{I\mu\nu}$
Universal Operators		
$\mathcal{O}_T = \frac{1}{2}(H^\dagger \overleftrightarrow{D}_\mu H)^2$	$\mathcal{O}_{HD} = (H^\dagger D^\mu H)^*(H^\dagger D_\mu H)$	$\mathcal{O}_{3G} = \frac{1}{3!}g_s f_{abc} G^{a\,\nu}_\mu G^b_{\nu\rho} G^{c\,\rho\mu}$
$\mathcal{O}_W = \frac{ig}{2}(H^\dagger \sigma^a \overleftrightarrow{D^\mu} H)D^\nu W^a_{\mu\nu}$	$\mathcal{O}_B = \frac{ig'}{2}(H^\dagger \overleftrightarrow{D^\mu} H)\partial^\nu B_{\mu\nu}$	$\mathcal{O}_{WB} = gg'(H^\dagger \sigma^I H)W^I_{\mu\nu}B^{\mu\nu}$
$\mathcal{O}_{HW} = ig(D^\mu H)^\dagger \sigma^a (D^\nu H)W^a_{\mu\nu}$	$\mathcal{O}_{HB} = ig'(D^\mu H)^\dagger (D^\nu H)B_{\mu\nu}$	$\mathcal{O}_{3W} = \frac{1}{3!}g\epsilon_{abc} W^{a\,\nu}_\mu W^b_{\nu\rho} W^{c\,\rho\mu}$
$\mathcal{O}_{2G} = \frac{1}{2}\left(D^\nu G^a_{\mu\nu}\right)^2$	$\mathcal{O}_{2B} = \frac{1}{2}\left(\partial^\rho B_{\mu\nu}\right)^2$	$\mathcal{O}_{2W} = \frac{1}{2}\left(D^\rho W^a_{\mu\nu}\right)^2$
and $\mathcal{O}_H, \mathcal{O}_6, \mathcal{O}_{BB}, \mathcal{O}_{WW}, \mathcal{O}_{GG}, \mathcal{O}_y = \sum_\psi \mathcal{O}_{y_\psi}$		
Non-Universal Operators that modify Z/W couplings to fermions		
$\mathcal{O}_{HL} = (iH^\dagger \overleftrightarrow{D}_\mu H)(\bar{L}\gamma^\mu L)$	$\mathcal{O}^{(3)}_{HL} = (iH^\dagger \sigma^a \overleftrightarrow{D}_\mu H)(\bar{L}\sigma^a\gamma^\mu L)$	$\mathcal{O}_{He} = (iH^\dagger \overleftrightarrow{D}_\mu H)(\bar{e}\gamma^\mu e)$
$\mathcal{O}_{HQ} = (iH^\dagger \overleftrightarrow{D}_\mu H)(\bar{Q}\gamma^\mu Q)$	$\mathcal{O}^{(3)}_{HQ} = (iH^\dagger \sigma^a \overleftrightarrow{D}_\mu H)(\bar{Q}\sigma^a\gamma^\mu Q)$	
$\mathcal{O}_{Hu} = (iH^\dagger \overleftrightarrow{D}_\mu H)(\bar{u}\gamma^\mu u)$	$\mathcal{O}_{Hd} = (iH^\dagger \overleftrightarrow{D}_\mu H)(\bar{d}\gamma^\mu d)$	
CP-odd operators		
$\mathcal{O}_{H\widetilde{W}} = (H^\dagger H)\widetilde{W}^I_{\mu\nu}W^{I\mu\nu}$	$\mathcal{O}_{H\widetilde{B}} = (H^\dagger H)\widetilde{B}_{\mu\nu}B^{\mu\nu}$	$\mathcal{O}_{\widetilde{W}B} = (H^\dagger \sigma^I H)\widetilde{W}^I_{\mu\nu}B^{\mu\nu}$
	$\mathcal{O}_{3\widetilde{W}} = \frac{1}{3!}g\epsilon_{abc} W^{a\,\nu}_\mu W^b_{\nu\rho}\widetilde{W}^{c\,\rho\mu}$	

Reduction to a minimal basis is achieved via integration by parts and field re-definitions, equivalent in practice to removing combinations proportional to the equations of motion. These imply relations between the operators of table 1; the most important ones being (Y denotes here hyper-charge)

$$\mathcal{O}_{HB} = \mathcal{O}_B - \frac{1}{4}\mathcal{O}_{BB} - \frac{1}{4}\mathcal{O}_{WB}\,, \qquad \mathcal{O}_{HW} = \mathcal{O}_W - \frac{1}{4}\mathcal{O}_{WW} - \frac{1}{4}\mathcal{O}_{WB} \tag{2}$$

$$\mathcal{O}_B = \frac{g'^2}{2}\sum_\psi Y_\psi \mathcal{O}_{H\psi} - \frac{g'^2}{2}\mathcal{O}_T\,, \qquad \mathcal{O}_T = \mathcal{O}_H - 2\mathcal{O}_{HD} \tag{3}$$

$$\mathcal{O}_W = \frac{g^2}{2}\Big[\left(\mathcal{O}_{y_u} + \mathcal{O}_{y_d} + \mathcal{O}_{y_e} + \text{h.c.}\right) - 3\mathcal{O}_H + 4\mathcal{O}_6 + \frac{1}{2}\sum_{\psi_L}\mathcal{O}^{(3)}_{H\psi_L}\Big]\,, \tag{4}$$

and similar expressions for $\mathcal{O}_{2W}$ and $\mathcal{O}_{2B}$ in terms of the products of $SU(2)$ and $U(1)$ SM currents. Eqs. (2-4) can be used to define minimal, non-redundant operator bases; for instance, in the context of Higgs physics, the operators $\mathcal{O}_H, \mathcal{O}_W, \mathcal{O}_B, \mathcal{O}_{HW}, \mathcal{O}_{HB}$ are retained at the expense of $\mathcal{O}_{HD}$, $\mathcal{O}_{WW}$, $\mathcal{O}_{WB}$, $\mathcal{O}^{(3)}_{HL}$, $\mathcal{O}_{HL}$ in what is known as the SILH basis [40], while in the opposite case we refer to the Warsaw basis [41].[1]

[1] In addition, the SILH basis gives preference to the operators $\mathcal{O}_{2W}$ and $\mathcal{O}_{2B}$, which are more easily found in universal BSM theories, while the Warsaw basis swaps them in terms of four-fermions operators.

These operators induce two types of effects: some that are proportional to the SM amplitudes and some that produce genuinely new amplitudes. The former are better accessed by high-luminosity experiments in kinematic regions where the SM is the largest. The most interesting example of this class for the LHC are Higgs couplings measurements in single-Higgs processes. The operators in the top panel of table 1 have the form $|H|^2 \times \mathcal{L}_{\rm SM}$, with $\mathcal{L}_{\rm SM}$ denoting operators in the SM Lagrangian, and imply small modifications $\propto v^2/\Lambda^2$ of the Higgs couplings to other SM fields, with respect to the SM value. These are often parametrised as rescalings of the SM rates, $\kappa_i^2 = \Gamma_i/\Gamma_i^{\rm SM}$ ($\Gamma^{\rm SM}$ the Higgs partial width into channel i) *assuming* the same Lorentz structure as that of the SM, i.e. providing an overall energy-independent factor. This is known as the kappa framework [42]. We discuss Higgs couplings in detail in sections 2 and 4 .

Among effects associated with new amplitudes, that cannot be put in correspondence with the κs, particularly interesting are BSM energy-growing effects. At dimension-6 level we find effects that grow at most quadratically with the energy. This implies a quadratic enhancement of the sensitivity to these effects, as we consider bins at higher and higher energy. This can be contrasted with high-intensity effects, whose sensitivity increases only with the square root of the integrated luminosity, and eventually saturates as systematics become comparable. High-energy effects are the ideal target of the HL and HE LHC programs, as we discuss in section 4. In section 8, we combine the results from the various EFT analyses and provide a global perspective on the HL and HE LHC sensitivity to EFT effects.

Ultimately, the goal of these global fits is to provide a model-independent framework to which large classes of specific models can be matched an analysed. We provide some example in section 8.

1.2.2 Light new physics: rare processes and new degrees of freedom

A complementary way to unveil BSM physics affecting the Higgs sector of Nature is the search for very rare processes involving the 125 GeV Higgs boson and for extended Higgs sectors.

The SM predicts several processes involving the Higgs boson to be very rare. Notable examples are the di-Higgs production, as well as the Higgs decays to first and second generation quarks and leptons. The search for these rare processes can unveil the presence of new degrees of freedom. Particularly, measurements of the di-Higgs production cross section (Sec. 3) will give constraints on the Higgs trilinear interaction, therefore providing information on electroweak symmetry breaking and allowing to set constraints on e.g. the nature of the phase transition between the trivial Higgs vacuum and the vacuum we observe at present (Sec. 3.6.2) and on the presence of extended Higgs sectors. The HL and HE stages of the LHC will be crucial to achieve this goal thanks to the relatively sizeable di-Higgs samples that will be produced: $\mathcal{O}(100\ \mathrm{K})$ at HL-LHC and $\mathcal{O}(2\ \mathrm{millions})$ at HE-LHC (compared to the $\mathcal{O}(6\ \mathrm{K})$ di-Higgs produced at Run 1 and 2 LHC). Furthermore, the branching ratios of SM rare Higgs decay modes such as $h \to \mu^+\mu^-$, $h \to Z\gamma$, and $h \to cc$ have been only mildly upper bounded by present LHC searches due in part to the low statistics ($h \to \mu^+\mu^-$, $h \to Z\gamma$) and, in part, to the background limited analyses ($h \to cc$). An important progress on these rare decay modes is expected at the HL and HE-LHC. For example, the HL-LHC will be able to discover and have a $(10-13)\%$ accuracy measurement of the di-muon decay mode (Sec. 2.3.8). Knowing the Higgs couplings to light quark and lepton generations will shed light on BSM flavor models and possibly on the SM flavor puzzle (Sec. 7).

Beyond rare SM Higgs processes, BSM models that contain new light degrees of freedom, X_i, generically predict rare exotic Higgs, decays $h \to X_i X_j$ or $h \to X_i\ \mathrm{SM}_j$ where SM_j is a SM particle (Secs. 6 and 9.1. For a review see e.g. [43]). A typical example is the Higgs decaying to light dark matter particles. Thanks to the tiny Higgs width (~ 4 MeV), even very feebly coupled new light particles can lead to relatively sizeable Higgs branching ratios that can be probed by the LHC in the future. On the one hand, the HL and HE-LHC will produce huge samples of Higgs bosons from its main production mode, gluon fusion ($\mathcal{O}(10^8)$ and $\mathcal{O}(10^9)$, respectively). This can allow the search for super rare and low background signatures. On the other hand, the sample of Higgs bosons produced from sub-leading production modes in association with other SM particles (e.g. tth) will be sizeable, increasing the discovery

prospects for rare and more background limited Higgs decay signatures. Therefore, the HL/HE-LHC Higgs exotic decay program can be uniquely sensitive to the existence of a broad range of new light weakly coupled particles (on condition that trigger and analysis thresholds will be kept relatively low, to allow capturing this set of soft signatures).

In many BSM theories, electroweak symmetry is broken not only by one Higgs boson, but by several degrees of freedom. Examples are supersymmetric theories, composite Higgs theories, as well as theories of neutral naturalness. Overall, extended Higgs sectors can lead to new interesting signatures that are not contained in the SM. The search for additional Higgs bosons is a high priority for current and future colliders. The ATLAS and CMS collaborations have performed several searches for heavy neutral and charged Higgs bosons during the first two runs of the LHC. At the same time, the LHCb collaboration (as well as ATLAS and CMS) has pursued several searches for new Higgs bosons with a mass below 125 GeV. The reach of all these searches will expand considerably in the future and, especially, at the HL and HE-LHC. In Secs. 9.2-9.4 and 9.8 of this report, we study the prospects for testing some of the most promising signatures. Most of the BSM models that predict the existence of an extended Higgs sector, also predict a 125 GeV Higgs with the interactions which are generically different from the SM predictions. As we will show in Secs. 9.5-9.7, the study of the interplay between new Higgs searches and Higgs coupling measurements will be a powerful tool to probe vast regions of parameter space of BSM theories with an extended electroweak symmetry breaking sector.

2 Higgs boson precision measurements[2]

2.1 Introduction

The large number of events expected in almost all Higgs boson measurement channels for the HL-LHC and HE-LHC will allow very precise measurements of the Higgs boson production cross sections and its couplings to gauge bosons and fermions. In many measurement channels, the expected overall statistical, experimental and theoretical uncertainties will be comparable in size. Therefore, a close interaction between the communities of the experimental and theoretical particle physicists will be needed in order to reach the best possible measurements of the Higgs boson properties.

Experimental sensitivity for the Higgs boson properties measurements is estimated by extrapolating the performance of the existing measurements to the HL-LHC data set, assuming the experiments will have a similar level of detector and triggering performance. Results are presented for two assumptions on the size of the experimental and theoretical systematic uncertainties that will be achievable by the time of HL-LHC (so called conservative and optimistic scenarios). Details on the extrapolation methodology and scenarios will be presented in Section 2.3.

Section 2.2 provides an overview of theoretical predictions for the Higgs boson production at 14 and 27 TeV and of the uncertainties that are expected to be reached by the time of the final HL-LHC and HE-LHC measurements. These predictions are used as input to sensitivity studies of the ATLAS and CMS Higgs boson cross section and coupling measurements in individual channels that are summarised in Section 2.3 and for the expectations for differential cross section measurements presented in Section 2.4. Section 2.5 puts emphasis on all measurements related to the top Yukawa coupling, as this is the largest Yukawa coupling in the Standard Model with a value close to unity and, hence, of special interest in understanding the Higgs mechanism and its relation to fermions. The combination of the expected measurements in ATLAS and CMS are presented in Section 2.6 together with an interpretation in the kappa-model [44, 42] in Section 2.7.

The kappa-framework is closely related to a non-linear EFT, and projections of measurements of EFT coefficients in a non-linear EFT are presented in Section 2.8 together with a translation of these results in terms of composite Higgs scenarios in section 2.9. Finally, probes of anomalous HVV interactions are discussed in Section 2.10.

2.2 Theoretical predictions for the Higgs boson production[3]

Cross-section predictions for the high-energy (HE) LHC, and their associated theoretical uncertainties, are discussed and shown in Section 2.2.1. Predictions are computed for a proton-proton collider with a pp centre-of-mass energy $\sqrt{s} = 27$ TeV and use a Higgs boson mass of $m_H = 125.09 \pm 0.5$ GeV. All other parameters are taken from YR4 [45], with exceptions noted where they are important. Projections of progress towards a reduction in theoretical uncertainties, on the timescale of the high-luminosity (HL) LHC (3 ab^{-1} of pp collisions at $\sqrt{s} = 14$ TeV), are discussed in Section 2.2.2. Tables summarising a detailed study of the dependence of the gluon-fusion cross section on the mass of the Higgs boson are presented in Section 2.2.4.

2.2.1 Cross sections for 13, 14 and 27 TeV HE-LHC

This section provides updated cross-sections for the LHC operating at energies of 13, 14 and 27 TeV. All predictions [46] include the latest theoretical input and supersede the older results in YR4 [45].

[2] Contact Editors: S. Alioli, M. Dührssen, P. Milenovic

[3] Contacts: K. Becker, C. Bertella, M. Bonvini, A. Calderon Tazon, J. Campbell, F. Caola, X. Chen, P. Francavilla, S. Frixione, R. Frederix, T. Gehrmann, N. Glover, Y. Haddad, V. Hirschi, A. Huss, S. Jones, A. Karlberg, M. Kerner, J. Lindert, G. Luisoni, G. Marchiori, S. Marzani, A. Massironi, B. Mistlberger, P. Monni, M. Moreno Llacer, A. Mück, D. Pagani, C. Palmer, C. Pandini, L. Perrozzi, S. Pozzorini, E. Re, L. Reina, H.S. Shao, L. Simon, B. Stieger, V. Theeuwes, F. Tramontano, M. Zaro

2.2.1.1 *Gluon fusion*

In this section we document cross section predictions for a standard model Higgs boson produced through gluon fusion in 27 TeV pp collisions. To derive predictions we include contributions based on perturbative computations of scattering cross sections as studied in Ref. [47]. We include perturbative QCD corrections through next-to-next-to-next-to-leading order (N^{3}LO), electroweak (EW) and approximated mixed QCD-electroweak corrections as well as effects of finite quark masses. The only modification with respect to YR4 [45] is that we now include the exact N^{3}LO heavy top effective theory cross section of Ref. [48] instead of its previous approximation. The result of this modification is only a small change in the central values and uncertainties. To derive theoretical uncertainties we follow the prescriptions outlined in Ref. [47]. We use the following inputs:

E_{CM}	27 TeV
$m_t(m_t)$	162.7 GeV
$m_b(m_b)$	4.18 GeV
$m_c(3\ \text{GeV})$	0.986 GeV
$\alpha_S(m_Z)$	0.118
PDF	PDF4LHC15_nnlo_100 [49]

(5)

All quark masses are treated in the $\overline{\text{MS}}$ scheme. To derive numerical predictions we use the program `iHixs` [50].

Sources of uncertainty for the inclusive Higgs boson production cross section have been assessed recently in refs. [47, 51, 52, 45]. Several sources of theoretical uncertainties were identified.

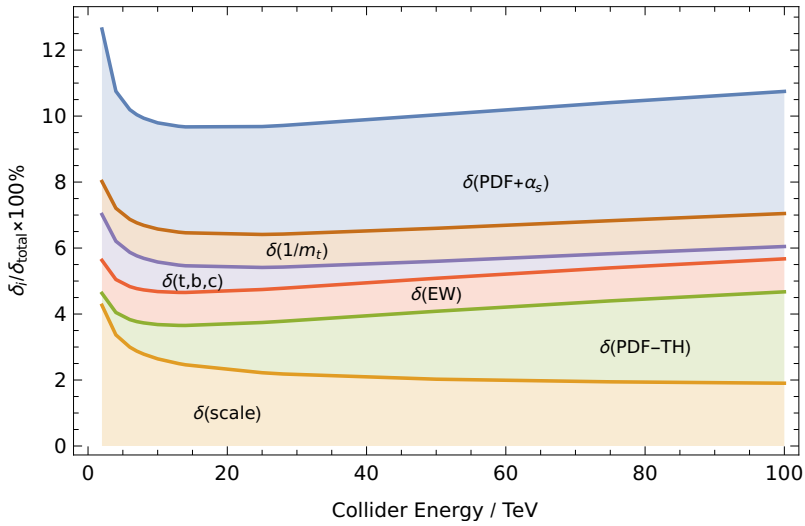

Fig. 1: The figure shows the linear sum of the different sources of relative uncertainties as a function of the collider energy. Each coloured band represents the size of one particular source of uncertainty as described in the text. The component $\delta(\text{PDF}+\alpha_S)$ corresponds to the uncertainties due to our imprecise knowledge of the strong coupling constant and of parton distribution functions combined in quadrature.

– Missing higher-order effects of QCD corrections beyond N^{3}LO (δ(scale)).
– Missing higher-order effects of electroweak and mixed QCD-electroweak corrections at and beyond $\mathcal{O}(\alpha_S\alpha)$ (δ(EW)).
– Effects due to finite quark masses neglected in QCD corrections beyond NLO (δ(t,b,c) and $\delta(1/m_t)$)

– Mismatch in the perturbative order of the parton distribution functions (PDF) evaluated at NNLO and the perturbative QCD cross sections evaluated at N^{3}LO (δ(PDF-TH)).

In the tables the linear sum of the effect of those uncertainties is referred to as δ(theory). In addition, the imprecise knowledge of the parton distribution functions and of the strong coupling constant play a dominant role. The individual size of these contributions can be seen in fig. 1 as a function of the collider energy [50]. As can be easily inferred the relative importance of the different sources of uncertainty is impacted only mildly by changing the centre of mass energy from 13 TeV to 27 TeV. Inclusive cross sections for $m_H = 125.09$ GeV are given in Table 2. As noted above, the exact treatment of N^{3}LO QCD corrections results in a small shift in the cross-section at 13 TeV, relative to the YR4 result, and a slight reduction in the overall theoretical uncertainty.

Table 2: Gluon fusion Higgs boson production cross sections and uncertainties as a function of the pp collider energy.

$\sqrt{s}$	σ	δ(theory)	δ(PDF)	$\delta(\alpha_s)$
13 TeV	48.61 pb	$^{+2.08\text{pb}}_{-3.15\text{pb}}$ $\left(^{+4.27\%}_{-6.49\%}\right)$	± 0.89 pb ($\pm 1.85\%$)	$^{+1.24\text{pb}}_{-1.26\text{pb}}$ $\left(^{+2.59\%}_{-2.62\%}\right)$
14 TeV	54.72 pb	$^{+2.35\text{pb}}_{-3.54\text{pb}}$ $\left(^{+4.28\%}_{-6.46\%}\right)$	± 1.00 pb ($\pm 1.85\%$)	$^{+1.40\text{pb}}_{-1.41\text{pb}}$ $\left(^{+2.60\%}_{-2.62\%}\right)$
27 TeV	146.65 pb	$^{+6.65\text{pb}}_{-9.44\text{pb}}$ $\left(^{+4.53\%}_{-6.43\%}\right)$	± 2.81 pb ($\pm 1.95\%$)	$^{+3.88\text{pb}}_{-3.82\text{pb}}$ $\left(^{+2.69\%}_{-2.64\%}\right)$

The dependence of the inclusive gluon-fusion cross-section on the Higgs boson mass at $\sqrt{s} = 14$ and 27 TeV is detailed at the end of this note in Section 2.2.4.

Impact of threshold and high-energy corrections

Recently, Ref. [53] has performed a study of the effects of simultaneous threshold and high-energy (small Bjorken x) resummations on the inclusive Higgs boson production cross section. In this brief section we summarise the main conclusions, while the numerical results will be discussed in the following section. For more details we refer the reader to Ref. [53]:

1. At different collider energies, it was found that the impact of threshold resummation amounts to about $+1\%$ on top of the N^{3}LO cross section [52]. The size of this effect is compatible with other estimates of the size of missing higher-order corrections.
2. Conversely, the inclusion of small-x resummation was found to increase the cross section by about one percent at 13 TeV, and by about $3\% - 4\%$ at 27 TeV, with respect to the N^{3}LO prediction. The correction grows even larger at higher energies, reaching about $+10\%$ for a 100 TeV pp collider. The inclusion of high-energy resummation affects differently the perturbative coefficient functions and the parton densities.
   – The effect on the coefficient functions is very moderate, and remains below the 1% level for different collider energies. This indicates that the production of a Higgs boson at present and future colliders does not probe very small values of the momentum fraction at which the coefficient functions are evaluated. In turn, this implies that currently and at future colliders PDFs are probed at intermediate values of x.
   – The parton densities receive a large correction from small-x resummation. Its effect is twofold: on one hand, the *evolution* of the gluon density is modified by the inclusion of small-x effects, and at average values of x probed in Higgs production this leads to a moderate effect on the parton densities at m_H (cf. Fig. 2.2 of Ref. [54]). On the other hand, the PDFs used in the double-resummed prediction of Ref. [53] (`NNPDF31sx_nnlonllx_as`

_0118 [54]) include small-x data from HERA, which Ref. [54] observes to require high-energy resummation for the fit to be robust. The fixed-order prediction of Ref. [53] instead uses a PDF set which fits the small-x HERA data without including high-energy resummation (NNPDF31sx_nnlo_as_0118 [54]). This results in sizeable differences in the parton distribution functions and drives the large correction to the N^{3}LO total cross section observed in Ref. [53].

Summarising, the sizeable corrections to the N^{3}LO prediction due to high-energy resummation observed in Ref. [53] are, to a large extent, due to the need for high-energy resummation in the PDF fit which are necessary to get a reliable description of small-x HERA data. Performing a fit without high energy resummation results in considerable tension with respect to low Q^2 HERA data. In order to corroborate these findings, and assess precisely the effect of high-energy resummation on parton distribution fits, it is important to make progresses in the theoretical knowledge of small-x dynamics. Furthermore, it would be desirable to include additional small-x collider data in the fits of parton distributions. We would like to encourage the PDF and theory community to further investigate these effects in view of future high energy colliders.

Predictions for double-resummed cross section

The setup is the same of the YR4 ($m_H = 125$ GeV, $m_t = 172.5$ GeV, $m_b = 4.92$ GeV, $m_c = 1.51$ GeV, $\alpha_s(m_Z^2) = 0.118$, $\mu_f = \mu_r = m_H/2$), with the only difference being that we do not use PDF4LHC but the NNPDF31sx_nnlonllx_as_0118 set of Ref. [54]. Since these resummed PDFs are available for a single value of α_s, we could not compute the α_s uncertainty in our result. The results are collected in Tab. 3.

For each value of the collider energy, we give the full N^{3}LO+N^{3}LL+LLx cross section which includes top, bottom and charm contributions (as discussed in Ref. [55]) and EW corrections included in the complete factorisation approach, i.e. as a $+5\%$ contribution. The breakdown of the individual terms contributing to the cross section (the main contribution assuming only top runs in the loop, the bottom+charm correction, and the EW correction) is presented in the third column. In the next columns, we present various sources of uncertainties, following Ref. [53]:

- Missing higher-order uncertainty (scale uncertainty) $\delta_{\rm scale}^{\rm 42var}$. It is the envelope of standard 7-point scale variations for each of the sub-leading variations of threshold resummed contributions, resulting in a total of 42 variation.
- PDF uncertainty $\delta_{\rm PDFs}$. This is the standard NNPDF Monte Carlo replica uncertainty, but it does not contain the α_s uncertainty, as previously discussed.
- Sub-leading small-x logarithms uncertainty $\delta_{\rm subl.logs}$. This uncertainty is computed as described in Refs. [53, 55], and it likely overestimates the effect of sub-leading contributions in the coefficient functions. However, as argued in Refs. [53, 55], this uncertainty can be considered as an estimate of the uncertainty from sub-leading contributions in the PDFs. In this respect, this provides an alternative to the uncertainty from missing higher-order PDFs adopted in YR4, which should thus not be included.

Additional uncertainties from missing $1/m_t^2$ effects, missing bottom+charm effects and sub-leading EW effects should be included according to the YR4 prescription. Since the N^{3}LO heavy-top result is matched to the exact small-x according to the construction of Ref. [55], the "truncation of the soft expansion" uncertainty discussed in YR4 should not be considered.

Finally, in the last column of the table we present the ratio of our resummed result with a purely fixed-order N^{3}LO cross section obtained with the same settings but using the NNLO parton distribution functions NNPDF31sx_nnlo_as_0118 of Ref. [54]. This is useful to understand how large the effect of resummation(s) in our prediction is. We see in particular that the effect (of small-x resummation) grows

Table 3: Values of the N^{3}LO+N^{3}LL+LLx gluon-fusion cross section for selected values of the pp collision energy and for a Higgs boson mass $m_H = 125$ GeV. We use the NNPDF31sx PDFs with $\alpha_s(m_Z^2) = 0.118$, $m_t = 173$ GeV, $m_b = 4.92$ GeV and $m_c = 1.51$ GeV.

$\sqrt{s}$	$\sigma_{\text{N}^3\text{LO+N}^3\text{LL+LL}x}$	$= \sigma_t + \Delta\sigma_{bc} + \Delta\sigma_{\text{EW}}$	$\delta^{42\text{var}}_{\text{scale}}$	δ_{PDFs}	$\delta_{\text{subl.logs}}$	$\frac{\sigma_{\text{N}^3\text{LO+N}^3\text{LL+LL}x}}{\sigma_{\text{N}^3\text{LO}}}$
13 TeV	48.93 pb	$(49.26 - 2.66 + 2.33)$ pb	$^{+4.0}_{-3.8}\%$	$\pm 1.2\%$	$\pm 1.8\%$	1.020
14 TeV	55.22 pb	$(55.56 - 2.96 + 2.63)$ pb	$^{+4.0}_{-3.8}\%$	$\pm 1.1\%$	$\pm 1.9\%$	1.023
27 TeV	151.6 pb	$(151.6 - 7.2 + 7.2)$ pb	$^{+4.0}_{-4.0}\%$	$\pm 1.0\%$	$\pm 2.3\%$	1.046

Table 4: VBF Higgs boson production cross-sections in pp collisions for centre-of-mass energies up to 27 TeV and a Higgs boson mass $m_H = 125.09$ GeV. The s-channel cross-section is the contribution from Higgs-strahlung diagrams with hadronic weak-boson decay [45].

$\sqrt{s}$ [TeV]	σ^{VBF} [fb]	Δ_{scale} [%]	$\Delta_{\text{PDF}\oplus\alpha_s}$ [%]	$\sigma^{\text{DIS}}_{\text{NNLO}}$ [fb]	δ_{ELWK} [%]	σ_γ [fb]	$\sigma_{s\text{-ch}}$ [fb]
13	3766	$^{+0.43}_{-0.33}$	± 2.1	3939	-5.3	35.3	1412
14	4260	$^{+0.45}_{-0.34}$	± 2.1	4460	-5.4	40.7	1555
27	11838	$^{+0.66}_{-0.36}$	± 2.1	12483	-6.2	129	3495

with the collider energy, reaching 4.6% at the HE-LHC. For any of the scales, approximately $+1\%$ of the effect of resummations is due to threshold resummation (in the coefficient functions), while the rest of the effect is due to small-x resummation, which mostly comes from the PDFs (see Ref. [53]) as discussed in the previous subsection.

2.2.1.2 *Vector boson fusion*

The vector-boson fusion (VBF) cross sections are computed with the same settings as in YR4 and reported in Tab. 4. The description of the setup can be found in the YR4 itself. The EW and photon cross sections have been computed using the `LUXqed_plus_PDF4LHC_nnlo_100` [56, 57] PDF set and hence the 13 and 14 TeV cross sections differ slightly from those reported in the YR4, where `NNPDF23_nlo_as_0118_qed` [58] was used instead. The QCD cross section was computed at NNLO with proVBFH [59, 60], while the EW and photon contributions have been computed at NLO with HAWK [61, 62, 63].

We note that the photon induced contribution is more reliably predicted here than was the case in the YR4 due to the LUXqed method. In particular the photon PDF should no longer be considered as a source of uncertainty as in eq. (I.5.7) in the YR4, as it is now constrained at the percent level. Quantitatively the photon induced contributions are reduced by about 30% compared to in the YR4.

The s-channel contributions at 13 and 14 TeV have on the other hand increased compared to the YR4 results. This is due to the updated set of parton distribution functions used for this prediction, i.e. `LUXqed_plus_PDF4LHC_nnlo_100` instead of `NNPDF23_nlo_as_0118_qed`. We also note that the relative size of the s-channel decreases as the collider energy increases - from 47% at 7 TeV to 30% at 27 TeV.

2.2.1.3 *VH production*

In Tabs. 5–14 we report the inclusive cross sections for associated production of a Higgs boson and a weak gauge boson $V = W, Z$, for pp collisions at 13, 14 and 27 TeV. The results have been obtained using HAWK, combining NNLO QCD and NLO EW corrections [64, 63, 65, 66, 67, 68, 69], by means of a multiplicative scheme, as described in the YR4 studies (eq. I.5.15 and I.5.16 of Ref. [45]). For

Table 5: Cross-section for the process $pp \to WH$. Both W^+ and W^- contributions are included. The photon contribution is not included. Results are given for a Higgs boson mass $m_H = 125.09$ GeV.

$\sqrt{s}$ [TeV]	$\sigma_{\text{NNLO QCD}\otimes\text{NLO EW}}$ [pb]	Δ_{scale} [%]	$\Delta_{\text{PDF}\oplus\alpha_s}$ [%]
13	1.358	$^{+0.51}_{-0.51}$	1.35
14	1.498	$^{+0.51}_{-0.51}$	1.35
27	3.397	$^{+0.29}_{-0.72}$	1.37

Table 6: Cross-section for the process $pp \to W^+H$. The photon contribution is not included. Results are given for a Higgs boson mass $m_H = 125.09$ GeV.

$\sqrt{s}$ [TeV]	$\sigma_{\text{NNLO QCD}\otimes\text{NLO EW}}$ [pb]	Δ_{scale} [%]	$\Delta_{\text{PDF}\oplus\alpha_s}$ [%]
13	0.831	$^{+0.74}_{-0.73}$	1.79
14	0.913	$^{+0.64}_{-0.76}$	1.78
27	1.995	$^{+0.43}_{-1.04}$	1.84

Table 7: Cross-section for the process $pp \to W^-H$. The photon contribution is not included. Results are given for a Higgs boson mass $m_H = 125.09$ GeV.

$\sqrt{s}$ [TeV]	$\sigma_{\text{NNLO QCD}\otimes\text{NLO EW}}$ [pb]	Δ_{scale} [%]	$\Delta_{\text{PDF}\oplus\alpha_s}$ [%]
13	0.527	$^{+0.59}_{-0.63}$	2.03
14	0.585	$^{+0.55}_{-0.68}$	1.98
27	1.402	$^{+0.36}_{-0.93}$	2.03

Table 8: Cross-section for the process $pp \to l^+\nu H$. The photon contribution is included, and also reported separately in the last column. Results are given for a Higgs boson mass $m_H = 125.09$ GeV.

$\sqrt{s}$ [TeV]	$\sigma_{\text{NNLO QCD}\otimes\text{NLO EW}}$ [pb]	Δ_{scale} [%]	$\Delta_{\text{PDF}\oplus\alpha_s}$ [%]	σ_γ
13	0.094	$^{+0.71}_{-0.70}$	1.72	$4.1\ 10^{-3}$
14	0.104	$^{+0.61}_{-0.73}$	1.70	$4.7\ 10^{-3}$
27	0.232	$^{+0.40}_{-0.97}$	1.72	$1.5\ 10^{-2}$

Table 9: Cross-section for the process $pp \to l^-\bar{\nu}H$. The photon contribution is included, and also reported separately in the last column. Results are given for a Higgs boson mass $m_H = 125.09$ GeV.

$\sqrt{s}$ [TeV]	$\sigma_{\text{NNLO QCD}\otimes\text{NLO EW}}$ [pb]	Δ_{scale} [%]	$\Delta_{\text{PDF}\oplus\alpha_s}$ [%]	σ_γ
13	0.0598	$^{+0.57}_{-0.60}$	1.94	$2.6\ 10^{-3}$
14	0.0666	$^{+0.52}_{-0.64}$	1.89	$3.1\ 10^{-3}$
27	0.1628	$^{+0.34}_{-0.87}$	1.90	$1.1\ 10^{-2}$

Table 10: Cross-section for the process $pp \to ZH$. The predictions for the $gg \to ZH$ channel are computed at LO, rescaled by the NLO K-factor in the $m_t \to \infty$ limit, and supplemented by the NLL$_{\rm soft}$ resummation. The photon contribution is omitted. Results are given for a Higgs boson mass $m_H = 125.09$ GeV.

$\sqrt{s}$ [TeV]	$\sigma_{\rm NNLO\ QCD\otimes NLO\ EW}$ [pb]	$\Delta_{\rm scale}$ [%]	$\Delta_{\rm PDF\oplus\alpha_s}$ [%]
13	0.880	$^{+3.50}_{-2.68}$	1.65
14	0.981	$^{+3.61}_{-2.94}$	1.90
27	2.463	$^{+5.42}_{-4.00}$	2.24

Table 11: Cross-section for the process $pp \to ZH$. The photon and $gg \to ZH$ contributions are omitted. Results are given for a Higgs boson mass $m_H = 125.09$ GeV.

$\sqrt{s}$ [TeV]	$\sigma_{\rm NNLO\ QCD\otimes NLO\ EW}$ [pb]	$\Delta_{\rm scale}$ [%]	$\Delta_{\rm PDF\oplus\alpha_s}$ [%]
13	0.758	$^{+0.49}_{-0.61}$	1.78
14	0.836	$^{+0.51}_{-0.62}$	1.82
27	1.937	$^{+0.56}_{-0.74}$	2.37

Table 12: Cross-section for the process $gg \to ZH$. Predictions are computed at LO, rescaled by the NLO K-factor in the $m_t \to \infty$ limit, and supplemented by the NLL$_{\rm soft}$ resummation. Results are given for a Higgs boson mass $m_H = 125.09$ GeV.

$\sqrt{s}$ [TeV]	$\sigma_{\rm NNLO\ QCD\otimes NLO\ EW}$ [pb]	$\Delta_{\rm scale}$ [%]	$\Delta_{\rm PDF\oplus\alpha_s}$ [%]
13	0.123	$^{+24.9}_{-18.8}$	4.37
14	0.145	$^{+24.3}_{-19.6}$	7.47
27	0.526	$^{+25.3}_{-18.5}$	5.85

Table 13: Cross-section for the process $pp \to l\bar{l}H$. The photon contribution is included, and reported separately in the last column. Results are given for a Higgs boson mass $m_H = 125.09$ GeV.

$\sqrt{s}$ [TeV]	$\sigma_{\rm NNLO\ QCD\otimes NLO\ EW}$ [pb]	$\Delta_{\rm scale}$ [%]	$\Delta_{\rm PDF\oplus\alpha_s}$ [%]	σ_γ
13	$2.97\ 10^{-2}$	$^{+3.49}_{-2.67}$	1.64	$1.4\ 10^{-4}$
14	$3.31\ 10^{-2}$	$^{+3.59}_{-2.92}$	1.89	$1.6\ 10^{-4}$
27	$8.32\ 10^{-2}$	$^{+5.39}_{-3.97}$	1.85	$5.4\ 10^{-4}$

Table 14: Cross-section for the process $pp \to \nu\bar{\nu}H$. Results are given for a Higgs boson mass $m_H = 125.09$ GeV.

$\sqrt{s}$ [TeV]	$\sigma_{\rm NNLO\ QCD\otimes NLO\ EW}$ [pb]	$\Delta_{\rm scale}$ [%]	$\Delta_{\rm PDF\oplus\alpha_s}$ [%]
13	0.177	$^{+3.50}_{-2.68}$	1.65
14	0.197	$^{+3.59}_{-2.92}$	1.89
27	0.496	$^{+5.41}_{-3.99}$	2.24

ZH production, the loop-induced $gg \to ZH$ channel has been computed at NLO+NLL, using a Born-improved Higgs effective field theory (HEFT) approach, and added linearly.

The contribution from photon-induced channels depends on the specific decay mode of the vector boson, and thus it has been removed from the total cross-sections, while it is instead included in the total result for the dedicated cross-sections where decay products are specified. In the latter cases, the individual photon-induced cross section is also separately reported.

The results at 27 and 14 TeV show a similar pattern of good perturbative convergence. There are two points that deserve some specific comment:

1. As can be evinced from the above tables, photon-induced contributions are relatively important in the $pp \to l^{\pm}\nu H$ case (where they amount to $\sim 4-7\%$ of the total cross section). For the $pp \to l\bar{l}H$ case instead, they contribute to only $\sim 4-7$ permille.
   We also notice that the relative weight of the photon-induced channel is computed more reliably than in the results previously obtained for the YR4 study: the changes in the values of σ_γ from the YR4 results (which also had large uncertainties) to those presented here are indeed non-negligible, and they are due to the fact that the photon PDF is now constrained significantly better, thanks to the LUXqed approach [56, 57]. We refer the reader to paragraph I.5.2.c of the YR4 for details on how this channel was treated previously. For the numbers in the new tables, the cross section for σ_γ was computed using the LUXqed_plus_PDF4LHC15_nnlo PDF set. For completeness, we also included an update for the 13 TeV cross sections using this PDF set.
2. As far as the loop-induced $gg \to ZH$ process is concerned, we remind that this channel starts contributing only at order α_S^2, hence it is part of the NNLO corrections to the $pp \to ZH$ cross section. Nevertheless, due to the gluon luminosity, its relative size is important, especially at large centre-of-mass energies. Due to the fact that it is a loop-induced channel, this contribution is known exactly (i.e. retaining finite values for the top mass) only at LO. However, because of its numerical size, and due to the fact that it contributes to the total cross section with a leading-order-like scale uncertainty, it is important to compute it at higher order. Exact NLO corrections to $gg \to ZH$ are not yet available. The numbers in the tables are obtained using a Born-improved HEFT approach, which essentially consists in computing the process at LO exactly, and rescaling it with the NLO/LO K-factor obtained in the $m_t \to \infty$ limit. NLL threshold effects have also been included. At order α_S^3 there are however many other gluon-gluon initiated sub-processes that are not yet calculated. It is reasonable to expect that for VH the correction to the loop induced process will be the first at order α_S^3 to be evaluated in the near future, so that this contribution can provide an order of magnitude estimate of the remaining perturbative uncertainty coming from the missing higher orders.

2.2.1.4 $t\bar{t}H$ and tH

Cross sections for $t\bar{t}H$ and $tH + \bar{t}H$ production at $\sqrt{s} = 14$ and 27 TeV are presented in Tables 15-17 and Tables 18-20 respectively. Results have been obtained using the same setup as in YR4, and considering three values for M_H, namely $M_H = 125.09 \pm 0.5$ GeV. The theoretical uncertainties from renormalisation and factorisation scale dependence, PDF, and α_s are calculated as explained in Sec. I.6.2 of YR4 [45], to which we refer for full details. $t\bar{t}H$ predictions include NLO QCD [70, 71, 72, 73, 74, 75, 76] and NLO QCD+EW corrections [75, 77, 76], while $tH + \bar{t}H$ predictions are accurate at NLO QCD only [78]. In both cases, `MadGraph5_aMC@NLO` [79, 80] has been employed for the computation of the cross sections. As expected, going to higher energies greatly enhances both $t\bar{t}H$ and $tH + \bar{t}H$ cross sections.

Table 15: NLO QCD+EW cross sections for $t\bar{t}H$ production at the 13 TeV LHC, taken from Ref. [45].

m_{H} [GeV]	$\sigma^{\mathrm{NLO}}_{\mathrm{QCD+EW}}$ [fb]	Scale [%]	α_s [%]	PDF [%]	PDF+α_s [%]
124.59	512.2	$^{+5.8}_{-9.2}$	2.0	3.0	3.6
125.09	506.5	$^{+5.8}_{-9.2}$	2.0	3.0	3.6
125.59	500.7	$^{+5.8}_{-9.2}$	2.0	3.0	3.6

Table 16: NLO QCD+EW cross sections for $t\bar{t}H$ production at the 14 TeV LHC.

m_{H} [GeV]	$\sigma^{\mathrm{NLO}}_{\mathrm{QCD+EW}}$ [fb]	Scale [%]	α_s [%]	PDF [%]	PDF+α_s [%]
124.59	619.3	$^{+6.1}_{-9.2}$	1.9	2.9	3.5
125.09	612.8	$^{+6.0}_{-9.2}$	1.9	2.9	3.5
125.59	605.6	$^{+6.1}_{-9.2}$	1.9	2.9	3.5

Table 17: NLO QCD+EW cross sections for $t\bar{t}H$ production at a 27 TeV proton–proton collider.

m_{H} [GeV]	$\sigma^{\mathrm{NLO}}_{\mathrm{QCD+EW}}$ [pb]	Scale [%]	α_s [%]	PDF [%]	PDF+α_s [%]
124.59	2.90	$^{+7.9}_{-9.0}$	1.8	2.1	2.8
125.09	2.86	$^{+7.8}_{-9.0}$	1.8	2.1	2.8
125.59	2.84	$^{+7.9}_{-9.0}$	1.8	2.1	2.8

Table 18: NLO QCD cross sections for the $t-$channel tH and $\bar{t}H$ production at the 13 TeV LHC, taken from Ref. [45].

m_{H} [GeV]	$\sigma_{t\mathrm{H}+\bar{t}\mathrm{H}}$ [fb]	Scale+FS [%]	α_s [%]	PDF [%]	PDF+α_s [%]	$\sigma_{t\mathrm{H}}$ [fb]	$\sigma_{\bar{t}\mathrm{H}}$ [fb]
124.59	74.52	$^{+6.6}_{-14.7}$	1.2	3.5	3.7	49.04	25.49
125.09	74.26	$^{+6.5}_{-14.7}$	1.2	3.5	3.7	48.89	25.40
125.59	74.09	$^{+6.5}_{-15.2}$	1.2	3.6	3.7	48.75	25.32

Table 19: NLO QCD cross sections for the $t-$channel tH and $\bar{t}H$ production at the 14 TeV LHC.

m_{H} [GeV]	$\sigma_{t\mathrm{H}+\bar{t}\mathrm{H}}$ [fb]	Scale+FS [%]	α_s [%]	PDF [%]	PDF+α_s [%]	$\sigma_{t\mathrm{H}}$ [fb]	$\sigma_{\bar{t}\mathrm{H}}$ [fb]
124.59	90.35	$^{+6.4}_{-14.6}$	1.2	3.4	3.6	59.15	31.21
125.09	90.12	$^{+6.4}_{-14.7}$	1.2	3.4	3.6	58.96	31.11
125.59	89.72	$^{+6.4}_{-14.8}$	1.2	3.4	3.6	58.70	31.02

Table 20: NLO QCD cross sections for the $t-$channel tH and $\bar{t}H$ production at a 27 TeV proton–proton collider.

m_{H} [GeV]	$\sigma_{t\mathrm{H}+\bar{t}\mathrm{H}}$ [fb]	Scale+FS [%]	α_s [%]	PDF [%]	PDF+α_s [%]	$\sigma_{t\mathrm{H}}$ [fb]	$\sigma_{\bar{t}\mathrm{H}}$ [fb]
124.59	419.0	$^{+5.0}_{-12.3}$	1.3	2.6	2.9	263.3	155.7
125.09	417.9	$^{+5.0}_{-12.5}$	1.3	2.6	2.9	262.8	155.1
125.59	416.4	$^{+5.0}_{-12.6}$	1.3	2.6	2.9	261.8	154.7

2.2.2 Projections of uncertainty reductions for the HL-LHC

This section discusses improvements to the theoretical predictions that may be possible on the timescale of the HL-LHC. Estimates of potential reductions in current theoretical uncertainties are made where possible and potential limiting factors identified.

2.2.2.1 Gluon fusion

Improving substantially on any of the current sources of uncertainty represents a major theoretical challenge that should be met in accordance with our ability to utilise said precision and with experimental capabilities. The computation of sub-leading mass and EW corrections is currently being addressed by several groups, and therefore it is likely to be achieved in the next decade. Although such computations will allow for a better control over some sources of uncertainty, their final impact on the full theoretical error is likely to be moderate as current estimates indicate. Another source of error that might improve in the forthcoming years is that related to the parton densities. In particular, the extraction of N^{3}LO PDFs would lead to the disappearance of the PDF-TH uncertainty. Similar considerations apply to the error on the strong coupling constant, that will be reduced due to more accurate extractions. Overall, the above progress would ultimately lead to a notable reduction of the uncertainties of Figure 1.

It is obvious that the future precision of experimental measurement of Higgs boson properties will challenge the theoretical community. Achieving a significant improvement of our current theoretical understanding of the Higgs boson and its interactions will inspire us to push the boundaries of our capabilities to predict and extract information. New ways of utilising quantum field theory in our endeavours have to be explored and our perturbative and non-perturbative understanding of hadron scattering processes has to evolve substantially. It is clear that this exciting task can only be mastered by a strong and active collider phenomenology community.

Impact of future precision of parton distribution function

It is a tantalising question to ask by how much one of the largest sources of uncertainty - the imprecise knowledge of PDFs - would be reduced if already all future LHC data were available. To this end a study was performed in ref. [38] (see also Section 2.2.5) that uses simulated future data with accordingly shrunken statistical uncertainties to constrain parton distribution functions. The authors used pseudo data corresponding to measurements of ATLAS, CMS and LHCb for key precision processes after $3ab^{-1}$ of integrated luminosity were collected at the High-Luminosity LHC at 14 TeV. They then performed a new fit according to the PDF4LHC15 framework [49] and studied the implications of their analysis. The resulting PDFs are readily available and can be used in order to estimate the impact of this future data on specific observables. Three scenarios were considered in this study that assume that experimental systematic uncertainties will shrink at different levels relative to the 8 TeV run of the LHC. Scenario 1, scenario 2 and scenario 3 assume that the future systematic uncertainty will be equal, shrunk by a factor 0.7 or a factor of 0.4 w.r.t to the 8 TeV run respectively.

Evaluating the inclusive Higgs boson production cross section with this simulated PDFs results in the PDF uncertainties summarised in Tab. 21. Note, that the central values stay unchanged and all other uncertainties are not afflicted by the change of PDFs. Even the most pessimistic scenario leads to a reduction of the PDF uncertainty by factor of two. However, this projections should be viewed only as a first estimate for the determination of PDFs from future measurements. Predicting the future development and correlation of systematic experimental uncertainties is non trivial and may differ strongly from observable to observable. PDF uncertainties may in the future also be adversely impacted by a more accurate treatment of theoretical uncertainties in the predictions of cross sections that serve as input for PDF extraction. Data incompatibilities may occur for various reasons. It is clear that an understanding of the structure of the proton at percent level accuracy is clearly a formidable task and rightly deserves significant research in the future.

Table 21: Uncertainty due to imprecise knowledge of PDFs estimated with current and simulated future PDFs for different scenarios and at different collider energies.

E_{CM}	Current	Scenario 1	Scenario 2	Scenario 3
13 TeV	$\pm 1.85\%$	$\pm 0.78\%$	$\pm 0.69\%$	$\pm 0.59\%$
14 TeV	$\pm 1.85\%$	$\pm 0.78\%$	$\pm 0.68\%$	$\pm 0.58\%$
27 TeV	$\pm 1.95\%$	$\pm 0.81\%$	$\pm 0.72\%$	$\pm 0.61\%$

2.2.2.2 Vector boson fusion

VBF Higgs boson production is currently known at a very high theoretical accuracy. In the structure-function approximation, the cross section has been computed fully inclusively at N^{3}LO accuracy in QCD. Fiducial calculations in the same approximation exist at NNLO accuracy in QCD. The only contribution which is currently unknown is the contribution from two-loop diagrams with gluon exchange between the two VBF quark lines. The conceptual difficulty is that it is a $2 \to 3$ process and that currently there are no methods available for evaluating two-loop diagrams with more than four external legs. It is realistic that such methods will become available before the HE-LHC is in operation. Beyond the VBF approximation, the full NLO corrections in both the strong and electroweak coupling have been computed. The electroweak contributions are of the same order as, or in certain phase space regions even larger than, the NNLO QCD corrections. Taking all of this into account, it has been estimated that the VBF cross section under typical VBF cuts has an accuracy at the 1% level. In order to connect these calculations to experimental measurements one would ideally need merged 2- and 3-jet NLO samples matched with the parton shower [81, 82] (NLOPS level) or even better a fully exclusive generator for VBF matched with the parton shower at NNLO (NNLOPS) . It is realistic that this will become available within the next few years and certainly before the HL-/HE-LHC phases.

2.2.2.3 VH production

The Higgs couplings to W and Z bosons are related by $SU(2)_L$ gauge invariance. As such, the measurement of the Higgs associated production with a W or a Z is complementary to the vector boson fusion process, as first considered in e^+e^- colliders in Ref. [83]. At the time of writing, the numbers shown in Section 2.2.1.3 are the best estimates available for the $pp \to VH$ contribution. As far as the ZH final state is concerned, due to the progress made in the last couple of years for the computation of top-mass effects at NLO in Higgs-boson pair production, it is foreseeable that, in the forthcoming years (definitely in the timescale of HL/HE LHC), an exact NLO result (including finite-m_t effects) will be available also for $gg \to ZH$. If one assumes that a pattern similar to what was found for di-higgs production [84] also holds for $gg \to ZH$, one can expect that the total NLO/LO K-factor will be slightly smaller than in the HEFT limit (from 1.9–2.0 to $\sim$1.6) and the final scale uncertainty for the $gg \to ZH$ cross section will decrease from 18–25% to about 15%.[4]

All the above results have been obtained for a stable Higgs boson. For the Higgs boson decay to bottom quarks, it is known that higher-order corrections to the m_{bb} line-shape are relevant, as shown in Ref. [85] and also recently confirmed in Ref. [86]. Although explicit studies are not available, one can expect that effects similar to those observed at 13–14 TeV in the region $m_{bb} < m_H$ will persist also at higher energies.

The matching of fixed-order corrections to parton showers (PS) is available for the $pp \to VH$ signal processes, at NLO as well as at NNLO [87, 88]. As for Higgs decays to bottom quarks, a fixed-order

[4] We stress that these numbers have been obtained as a back-of-the-envelope estimate through a comparison with di-higgs production.

study [86] suggests that higher-order corrections to the m_{bb} shape are not always very well modelled by a LO + parton shower treatment of the $H \to b\bar{b}$ decay. Event generators as the one developed in Ref. [88], and improvements thereof for the treatment of radiation off b-quarks [89], will allow one to assess this issue in the forthcoming years. A solid prediction of the $H \to b\bar{b}$ decay, also matched to parton-showers, can definitely be expected in the timescale of HL/HE LHC.

Furthermore, once the exact $gg \to ZH$ computation at NLO will be completed, a NLO matching to parton-shower will be straightforward to achieve, thereby improving on the currently available more advanced treatments, where a LO-merging of the exact matrix elements for $gg \to ZH$ and $gg \to ZH$+1-jet is performed.

Finally, as for the VH and VHJ event generators, recently there has been also the completion of the NLO EW corrections matched to the parton shower [90] showing once again the relevance of the EW corrections for the distributions for both the fixed order and the matched predictions.

2.2.2.4 $t\bar{t}H$ and tH

The cross sections for $t\bar{t}H$ and tH production are known at NLO accuracy in QCD [70, 72, 91] and, in the case of $t\bar{t}H$, NLO EW corrections have also been calculated [75, 77]. The corresponding theoretical uncertainty is of the order of 10–15% and is mainly induced by the residual scale dependence and, to a lesser extent, by PDF uncertainties. A drastic improvement can only come from the calculation of the NNLO QCD corrections. Given the ongoing rapid progress in cross section calculations with NNLO accuracy in QCD, it is foreseeable that NNLO QCD corrections to $t\bar{t}H$ and tH will become available in the next decade. In this scenario it is reasonable to expect a factor-two improvement of the theoretical accuracy.

On the other hand, the extraction of the $t\bar{t}H$ signal is at the moment mainly limited by the theoretical uncertainties in the modelling of the background, mainly $t\bar{t}b\bar{b}$ and $t\bar{t}W$+jets, via Monte Carlo generators. The reliable assessment of the related uncertainties and their further reduction are the main goals of an ongoing campaign of theoretical studies within the HXSWG. On a time scale of 5–10 years such background uncertainties may be reduced by a factor two to three.

2.2.3 Predictions for boosted Higgs production

The HL and HE LHC upgrades would allow for in-depth analyses of high-p_t tail of the Higgs transverse momentum distribution. This region is particularly interesting as it is very sensitive to BSM physics in the Higgs sector. For example, measures in the boosted region would allow one to lift the degeneracy between ggH and ttH couplings, and more in general to probe the internal structure of the ggH interaction. In this section, we report theoretical predictions for boosted Higgs production.

We first present results for the 13-TeV LHC. In Fig. 2(left) we show the cumulative Higgs transverse momentum distribution, defined as

$$\Sigma(p_t^H) = \int_{p_t^H}^{\infty} \frac{d\sigma}{dp_t},$$

for the main production channels. The ggF prediction is obtained by rescaling the exact NLO with the NNLO $K-$factor in the $m_t \to \infty$ approximation, and it does not contain EW corrections. The VBF and VH predictions include NNLO QCD and NLO EW corrections, while the $t\bar{t}H$ prediction includes NLO QCD and EW corrections. In Fig. 2(right), we show the relative importance of the different production mechanisms.[5] As it is well known, at high p_t the ggF channel becomes somewhat less dominant. Still,

[5] The small feature around $p_t \sim 750$ GeV in the ggF channel is due to lack of statistics in the theoretical simulation and it is not a genuine physical feature.

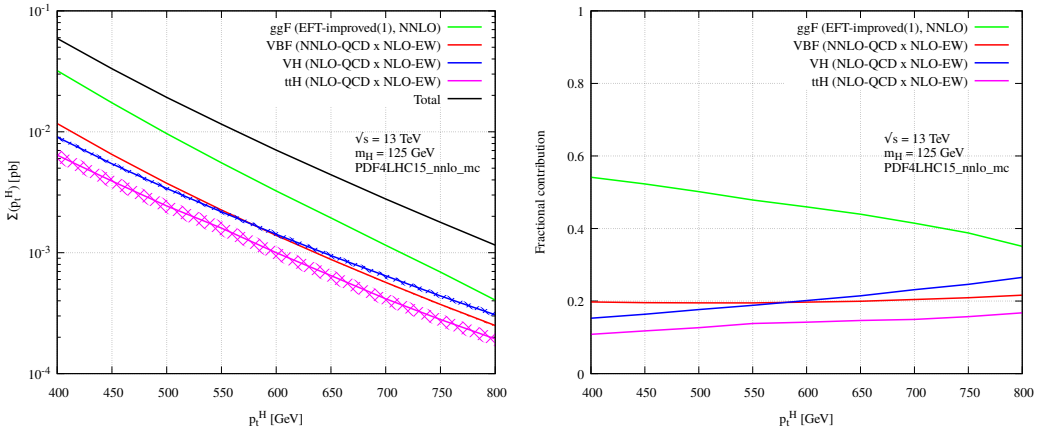

Fig. 2: Boosted Higgs prediction at the 13-TeV LHC. Left: cumulative transverse momentum distribution. Right: relative importance of different production mechanisms. See text for details.

radiative corrections strongly enhance this channel, which remains the dominant one in the TeV region. A very similar picture is expected for the HL-LHC.

Figs. 3 and 4 show similar predictions for the HE-LHC. In Fig. 3, all predictions are LO. At high

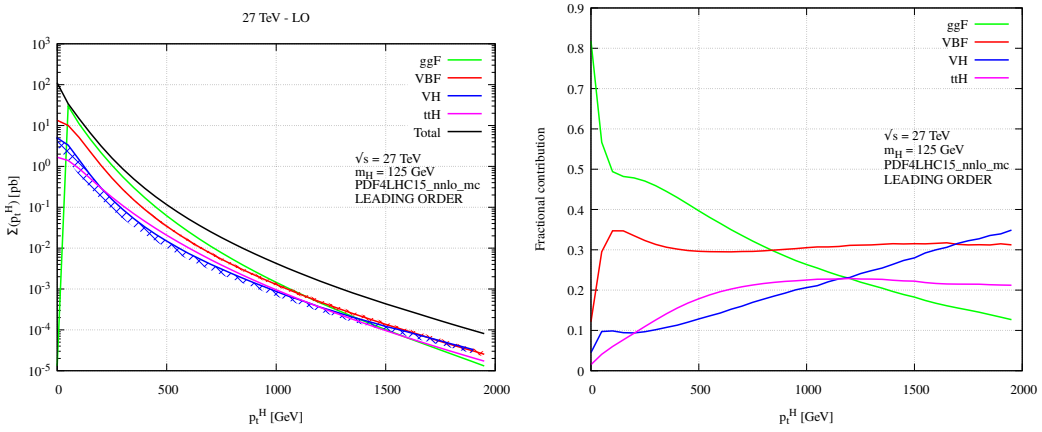

Fig. 3: LO boosted Higgs prediction at the 27-TeV LHC. Left: cumulative transverse momentum distribution. Right: relative importance of different production mechanisms. See text for details.

p_t, the ggF channel become sub-dominant compared to the other ones. VBF becomes the dominant channel around $p_t \sim 1$ TeV, and VH around $p_t \sim 2$ TeV. In the TeV region, the $t\bar{t}H$ channel becomes larger than ggF.

This picture is however significantly altered by radiative correction, whose size and impact is very different for different channels. This is shown in Fig. 4, where predictions include radiative corrections. More precisely, the VBF, VH and $t\bar{t}H$ predictions have the same accuracy as the ones in Fig. 2. The ggF prediction contains exact LO mass effects rescaled by the NLO $K-$factor in the m_t approximation. This is expected to provide an excellent approximation of the exact NLO result. Radiative corrections enhance the relative importance of the ggF and $t\bar{t}H$ channels, which still dominate over VBF well into

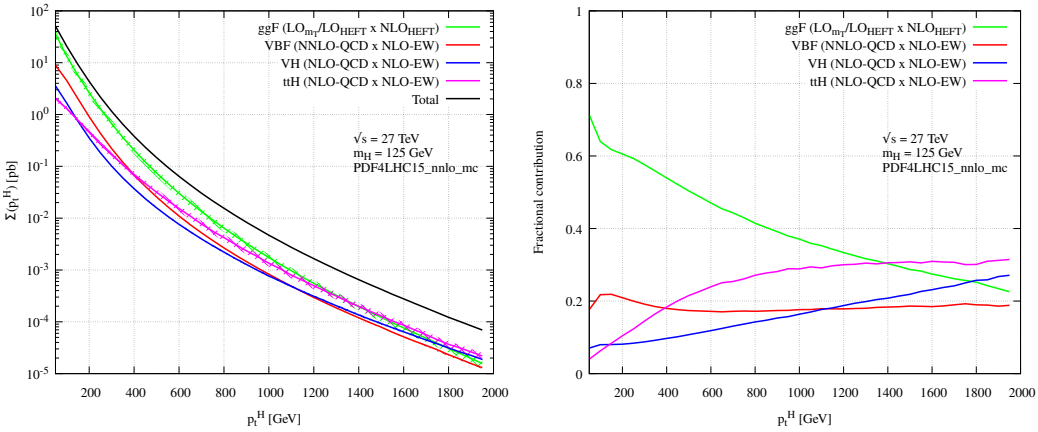

Fig. 4: Boosted Higgs prediction at the 27-TeV LHC, including radiative corrections. Left: cumulative transverse momentum distribution. Right: relative importance of different production mechanisms. See text for details.

the multi-TeV region. At large $p_t \sim 1.5$ TeV, the $t\bar{t}H$ channel becomes the dominant one.

Obtaining accurate and precise theoretical predictions in the boosted region is very challenging. Nevertheless, it is natural to expect progress in the timescale for the HL and HE LHC upgrades. This would allow for a proper scrutiny of the structure of Higgs interactions in the multi-TeV regime.

2.2.4 *Dependence of gluon-fusion cross section at* 14 *and* 27 *TeV on* m_H

The dependence of the inclusive gluon-fusion cross-section on the Higgs boson mass is shown in Tables 22 and 23, for pp collisions at $\sqrt{s} = 14$ and 27 TeV, respectively.

2.2.5 *PDF uncertainty expectations at the HE/HL-LHC*[6]

PDFs in the HL-LHC era. The detailed understanding of the quark and gluon structure of the proton, quantified by the parton distribution functions (PDFs) [92, 93, 94], is an essential ingredient for the theoretical predictions at hadron colliders. PDF uncertainties represent one of the dominant theoretical systematic errors both for direct searches of new physics beyond the Standard Model (BSM) [95] as well as in the profiling of the Higgs boson sector [45]. Therefore, improving our knowledge of the proton structure is an essential task for the high-precision physics program to be carried out at future runs of the LHC, including the HL-LHC era.

Modern global PDF fits [96, 97, 98, 99] include a wide range of LHC measurements in processes such as the production of jets, weak gauge bosons, and top quark pairs, among others. Recent breakthroughs in the calculation of NNLO QCD and NLO QED and electroweak corrections to most PDF-sensitive processes have been instrumental in allowing for the full exploitation of the information provided by the LHC measurements. The impact of high-precision LHC data combined with state-of-the art perturbative calculations has been quantified for many of the processes of interest, such as top-quark pair production [100, 101], the transverse momentum spectrum of Z bosons [102], direct photon production [103, 104], D meson production in the forward region [105, 106, 107], W production in association with charm quarks [108, 109], and inclusive jet production [110, 111].

From the point of view of PDF determinations, the availability of the immense data samples at the

[6] Contacts: R. Abdul Khalek, S. Bailey, J. Gao, L. Harland-Lang, J. Rojo

Table 22: The gluon-fusion cross-section in pp collisions at $\sqrt{s} = 14$ TeV, for different values of the Higgs boson mass m_H.

m_H [GeV]	Cross Section [pb]	+ δTh. [%]	- δTh. [%]	$\pm\delta$(PDF+α_S) [%]	$\pm\delta\alpha_S$ [%]	$\pm\delta$ PDF [%]
125.09	54.72	4.29	−6.46	3.20	2.61	1.85
124.59	55.10	4.29	−6.48	3.20	2.61	1.86
125.59	54.34	4.28	−6.45	3.20	2.61	1.85
120.00	58.85	4.37	−6.61	3.23	2.63	1.87
120.50	58.42	4.37	−6.60	3.22	2.63	1.87
121.00	58.00	4.36	−6.58	3.22	2.63	1.87
121.50	57.56	4.35	−6.57	3.22	2.62	1.86
122.00	57.15	4.34	−6.55	3.22	2.62	1.86
122.50	56.75	4.33	−6.54	3.21	2.62	1.86
123.00	56.35	4.32	−6.52	3.21	2.62	1.86
123.50	55.95	4.31	−6.51	3.21	2.61	1.86
124.00	55.56	4.30	−6.49	3.21	2.61	1.86
124.10	55.48	4.30	−6.49	3.20	2.61	1.86
124.20	55.41	4.30	−6.49	3.20	2.61	1.86
124.30	55.33	4.30	−6.49	3.20	2.61	1.86
124.40	55.25	4.30	−6.48	3.20	2.61	1.86
124.50	55.17	4.30	−6.48	3.20	2.61	1.86
124.60	55.10	4.29	−6.48	3.20	2.61	1.86
124.70	55.02	4.29	−6.47	3.20	2.61	1.86
124.80	54.94	4.29	−6.47	3.20	2.61	1.86
124.90	54.86	4.29	−6.47	3.20	2.61	1.86
125.00	54.79	4.29	−6.47	3.20	2.61	1.86
125.10	54.71	4.29	−6.46	3.20	2.61	1.85
125.20	54.64	4.28	−6.46	3.20	2.61	1.85
125.30	54.56	4.28	−6.46	3.20	2.61	1.85
125.40	54.48	4.28	−6.45	3.20	2.61	1.85
125.50	54.41	4.28	−6.45	3.20	2.61	1.85
125.60	54.33	4.28	−6.45	3.20	2.61	1.85
125.70	54.26	4.28	−6.44	3.20	2.61	1.85
125.80	54.18	4.27	−6.44	3.20	2.60	1.85
125.90	54.11	4.27	−6.44	3.20	2.60	1.85
126.00	54.03	4.27	−6.44	3.20	2.60	1.85
126.50	53.66	4.26	−6.42	3.19	2.60	1.85
127.00	53.29	4.25	−6.41	3.19	2.60	1.85
127.50	52.92	4.25	−6.40	3.19	2.60	1.85
128.00	52.56	4.24	−6.38	3.19	2.60	1.85
128.50	52.20	4.23	−6.37	3.18	2.59	1.85
129.00	51.85	4.22	−6.35	3.18	2.59	1.85
129.50	51.50	4.21	−6.34	3.18	2.59	1.84
130.00	51.15	4.20	−6.33	3.18	2.59	1.84

HL-LHC will permit a significant extension of the kinematic coverage of PDF-sensitive measurements as well as a marked improvement in their statistical and systematic uncertainties. In this contribution, we

Table 23: The gluon-fusion cross-section in pp collisions at $\sqrt{s} = 27$ TeV, for different values of the Higgs boson mass m_H.

m_H [GeV]	Cross Section [pb]	+ δTh. [%]	- δTh. [%]	$\pm\delta$(PDF+α_S) [%]	$\pm\delta\alpha_S$ [%]	$\pm\delta$ PDF
125.09	146.65	4.53	−6.43	3.30	2.66	1.95
124.59	147.55	4.55	−6.45	3.30	2.67	1.95
125.59	145.75	4.52	−6.42	3.30	2.66	1.95
120.00	156.35	4.64	−6.60	3.33	2.69	1.97
120.50	155.36	4.63	−6.58	3.33	2.69	1.97
121.00	154.36	4.62	−6.56	3.33	2.69	1.97
121.50	153.38	4.61	−6.55	3.32	2.68	1.96
122.00	152.41	4.60	−6.54	3.32	2.68	1.96
122.50	151.45	4.59	−6.52	3.32	2.68	1.96
123.00	150.50	4.58	−6.50	3.31	2.68	1.96
123.50	149.56	4.57	−6.49	3.31	2.67	1.96
124.00	148.64	4.56	−6.47	3.31	2.67	1.95
124.10	148.45	4.56	−6.47	3.31	2.67	1.95
124.20	148.27	4.56	−6.46	3.31	2.67	1.95
124.30	148.08	4.55	−6.46	3.31	2.67	1.95
124.40	147.90	4.55	−6.46	3.31	2.67	1.95
124.50	147.72	4.55	−6.46	3.31	2.67	1.95
124.60	147.53	4.55	−6.45	3.30	2.67	1.95
124.70	147.35	4.54	−6.45	3.30	2.67	1.95
124.80	147.17	4.54	−6.44	3.30	2.67	1.95
124.90	146.99	4.54	−6.44	3.30	2.67	1.95
125.00	146.81	4.54	−6.44	3.30	2.67	1.95
125.10	146.63	4.53	−6.43	3.30	2.66	1.95
125.20	146.45	4.53	−6.43	3.30	2.66	1.95
125.30	146.27	4.53	−6.43	3.30	2.66	1.95
125.40	146.09	4.53	−6.42	3.30	2.66	1.95
125.50	145.91	4.52	−6.42	3.30	2.66	1.95
125.60	145.73	4.52	−6.42	3.30	2.66	1.95
125.70	145.55	4.52	−6.41	3.30	2.66	1.95
125.80	145.37	4.52	−6.41	3.30	2.66	1.95
125.90	145.20	4.52	−6.41	3.30	2.66	1.95
126.00	145.02	4.51	−6.40	3.30	2.66	1.95
126.50	144.14	4.50	−6.39	3.29	2.66	1.94
127.00	143.26	4.49	−6.37	3.29	2.66	1.94
127.50	142.40	4.48	−6.36	3.29	2.65	1.94
128.00	141.54	4.48	−6.34	3.28	2.65	1.94
128.50	140.69	4.47	−6.33	3.28	2.65	1.94
129.00	139.84	4.46	−6.31	3.28	2.65	1.93
129.50	139.00	4.46	−6.30	3.27	2.64	1.93
130.00	138.18	4.45	−6.29	3.27	2.64	1.93

summarise the main results of our PDF projections for the HL-LHC era presented in [38]. The main idea is to quantify the impact of the future HL–LHC measurements on the proton PDFs and their uncertainties,

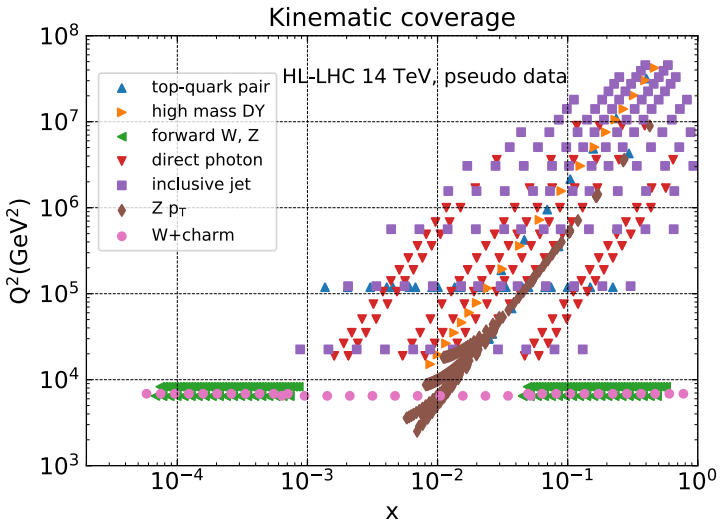

Fig. 5: The kinematic coverage in the (x, Q^2) plane of the HL–LHC pseudo-data.

with emphasis on their implications for Higgs physics. Specifically, we quantify the constraints of the HL–LHC pseudo-data on the PDF4LHC15 set [112, 113, 114, 115] by means of the Hessian Profiling method [116] (see also [117]). We choose the PDF4LHC15 set since it broadly represents the state-of-the-art understanding of the proton structure.

In Fig. 5 we show the kinematic coverage in the (x, Q^2) plane of the HL–LHC pseudo-data included in this analysis. As indicated there, we have simulated pseudo-data for the following processes: top quark pair production, high-mass and forward Drell-Yan W, Z production, direct photon and inclusive jet production, the transverse momentum of Z bosons, and the production of W bosons in association with charm quarks. The HL–LHC pseudo-data therefore spans a wide region in the kinematic plane, namely $6 \times 10^{-5} < x < 0.7$ and 40 GeV $< Q < 7$ TeV. In particular, one sees that the HL-LHC coverage of the large-x region, where current PDF fits exhibit large uncertainties, is markedly improved as compared to available LHC measurements.

Results. As an illustration of the impact of individual sets of HL-LHC pseudo-data, in Fig. 6 we show the comparison between the HL–LHC projected measurements and the theoretical predictions for the lepton rapidity distribution in forward W+charm production and for the invariant mass $m_{t\bar{t}}$ distribution in top-quark pair production. These two particular datasets probe the poorly-known strange quark and the gluon at large-x, respectively. The theory calculations are shown both before (PDF4LHC15) and after profiling. In the bottom panel, we show the same results normalised to the central value of the original theory calculation. In both cases we see that the expected precision of the HL-LHC measurements is rather higher than the current PDF uncertainties, and therefore we observe a marked improvement once they are included in PDF4LHC15 via the Hessian profiling.

In this study we have considered three different scenarios for the experimental systematic uncertainties of the HL–LHC pseudo-data. These scenarios, ranging from more conservative to more optimistic, differ among them in the reduction factor applied to the systematic errors of the reference 8 TeV or 13 TeV measurements, see [38] for more details. In particular, in the optimistic scenario we assume a reduction of the systematic errors by a factor 2.5 (5) as compared to the reference 8 TeV (13 TeV) measurements, while for the conservative scenario we assume no reduction in systematic errors with respect to the 8 TeV reference. Reassuringly, we obtain that the main results of our study depend only mildly in the specific assumption for the values of this reduction factor.

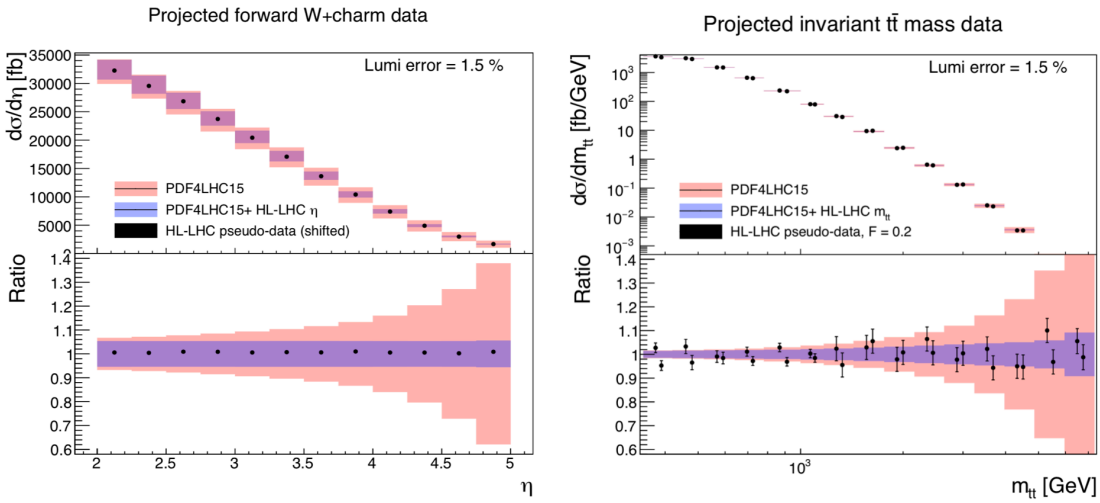

Fig. 6: Comparison between the HL–LHC pseudo-data and the theoretical predictions for forward $W+$charm production (left) and for the invariant mass $m_{t\bar{t}}$ distribution in top-quark pair production (right). The theory calculations are shown both before (PDF4LHC15) and after profiling.

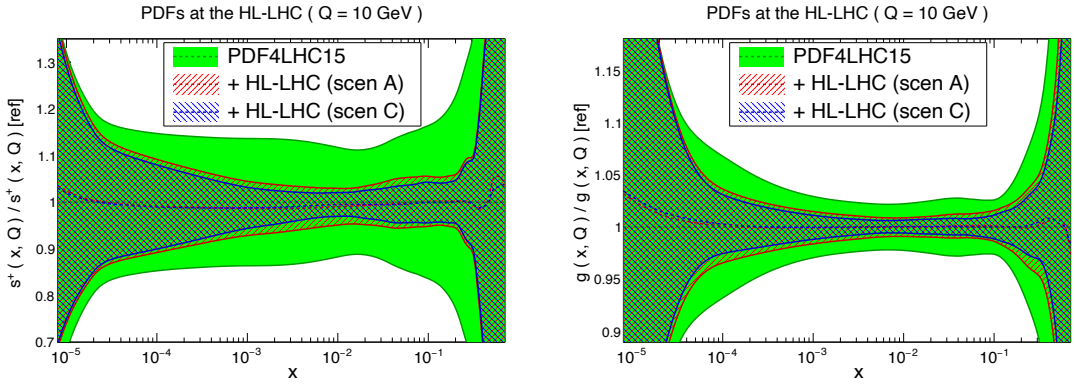

Fig. 7: Comparison of the PDF4LHC15 set with the profiled sets with HL–LHC pseudo-data. We show the strange (left) and gluon (right) PDFs normalised to the central value of the baseline.

In Fig. 7 we compare the PDF4LHC15 set with the strange quark and gluon PDFs obtained once the entire set of HL-LHC pseudo-data summarised in Fig. 5 has been included via profiling. We show results both in the conservative (A) and optimistic (C) scenarios for the projections of the experimental systematic uncertainties. We observe that the impact of the HL–LHC pseudo-data is reasonably similar in both scenarios. This is due to the fact that we have chosen those processes which will benefit from a significant improvement in statistics, independent of the specific assumption about the systematic errors. These then tend to lie in kinematic regions where the PDFs themselves are generally less well determined. We also observe a marked reduction of the PDF uncertainties in all cases. In the case of the gluon PDF, there is an improvement of uncertainties in the complete relevant range of momentum fraction x. This is a direct consequence of the fact that we have included several HL–LHC processes that have direct sensitivity to the gluon content of the proton, including jet, direct photon, and top quark pair production, as well as the transverse momentum of Z bosons. As we discuss next, this has direct implications for the phenomenology of Higgs boson production.

Table 24: The reduction of the PDF uncertainties as compared to the PDF4LHC15 baseline for different initial partonic combinations in the optimistic (conservative) scenario.

Ratio to baseline	$10\text{ GeV} \leq M_X \leq 40\text{ GeV}$	$40\text{ GeV} \leq M_X \leq 1\text{ TeV}$	$1\text{ TeV} \leq M_X \leq 6\text{ TeV}$
gluon-gluon	0.50 (0.60)	0.28 (0.40)	0.22 (0.34)
quark-quark	0.74 (0.79)	0.37 (0.46)	0.43 (0.59)
quark-antiquark	0.71 (0.76)	0.31 (0.40)	0.50 (0.60)

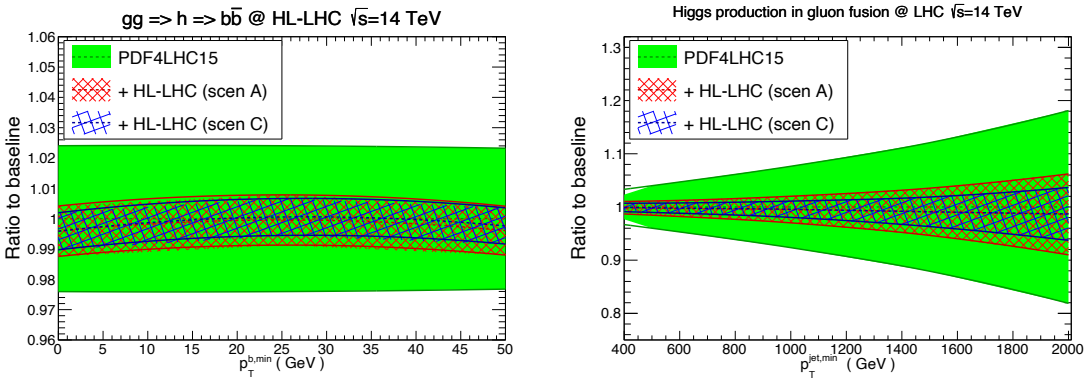

Fig. 8: Comparison of the predictions for SM Higgs production cross-sections at $\sqrt{s} = 14$ TeV between the PDF4LHC15 baseline and the profiled PDF sets with HL–LHC pseudo–data.

Implications for Higgs physics. In Table 24 we indicate the reduction of the PDF uncertainties in comparison to the PDF4LHC15 baseline for different initial partonic combinations (that is, a value of 1 corresponds to no improvement). Results are presented for three different bins of the invariant mass M_X of the produced system for the three initial states relevant for Higgs production: gluon-gluon (for $gg \to h$ and $t\bar{t}h$), quark-quark (for vector boson fusion) and quark-antiquark (for associated Wh and Zh production). The values shown outside (inside) the brackets correspond to the optimistic (conservative) scenario. We can see that for the M_X region relevant for the SM Higgs boson production, as well as for related BSM Higgs-like scalars, namely $40\text{ GeV} \leq M_X \leq 1\text{ TeV}$, the HL-LHC pseudo-data leads to a reduction by almost a factor four in the optimistic scenario in the gg channel, and around a factor three in the $q\bar{q}$ and qq channels. This implies that precision calculations of Higgs production at the HL-LHC should be possible with significantly reduced PDF uncertainties compared to current state-of-the-art predictions.

To illustrate this improvement, in Fig. 8 we present the comparison of the predictions for SM Higgs production at $\sqrt{s} = 14$ TeV between the PDF4LHC15 baseline and the profiled PDF sets. Specifically, we show Higgs boson production in gluon fusion with heavy top quark effective theory, both inclusive and decaying into $b\bar{b}$ as a function of $p_T^{b,\min}$ (left), and then in association with a hard jet as a function of its transverse momentum $p_{\rm T}^{\rm jet,min}$ (right). The calculations have been performed using `MCFM8.2` with leading-order matrix elements. The marked reduction of PDF uncertainties is consistent with the values reported in Table 24.

Finally, there are two caveats to be added concerning this study. First we have only considered a subset of all possible measurements of relevance for PDF fits at HL–LHC. Second, possible data

incompatibility has not been accounted for fully. These may strengthen and weaken, respectively, the constraining powers of future LHC data on PDFs.

The results of this study are made publicly available in the LHAPDF6 format [118], for the three scenarios that have been considered, and can be downloaded from:

```
https://data.nnpdf.science/HLLHC_YR/PDF4LHC15_nnlo_hllhc_scen1.tgz
https://data.nnpdf.science/HLLHC_YR/PDF4LHC15_nnlo_hllhc_scen2.tgz
https://data.nnpdf.science/HLLHC_YR/PDF4LHC15_nnlo_hllhc_scen3.tgz
```

2.3 Overview of experimental analysis for the Higgs boson measurement channels[7]

2.3.1 Extrapolation assumptions

The results presented in this Section are based on the extrapolation to an expected integrated luminosity of 3000 fb^{-1} of the corresponding ATLAS and CMS Run-2 results. For some of the Higgs decay final states (ATLAS: WW^*, $Z\gamma$, $t\bar{t}H$, $\tau\tau$; CMS: WW^*, $Z\gamma$, $\gamma\gamma$, ZZ^*, $t\bar{t}H$, $\tau\tau$, $b\bar{b}$ and $\mu\mu$) the extrapolation is performed from results obtained with the 2015-2016 36 fb^{-1} datasets; the remaining final state analyses (ATLAS: $\gamma\gamma$, ZZ^*, $b\bar{b}$ and $\mu\mu$) use the results based on the 2015+2016+2017 80 fb^{-1} data samples. The starting points of the extrapolated results are measurements based on datasets of size $\mathcal{O}(1\%)$ of the expected HL-LHC integrated luminosity. The extrapolations are in this regard very limited with respect to the potential reach of the real HL-LHC analyses, which large statistics will allow to probe corners of the phase space inaccessible at the LHC Run-2.

In addition to the increase in integrated luminosity, the ATLAS extrapolations also account for the increase of signal and background cross-sections from $\sqrt{s}$ = 13 TeV to 14 TeV. In those cases, the signal yields have been scaled according to the Higgs boson production cross sections values at 13 and 14 TeV, as reported in Ref. [45]. Similarly, the background yields have been scaled according to the parton luminosity ratio between 13 and 14 TeV, as reported in Ref. [42], by taking into account whether the background process is predominantly quark pair or gluon pair initiated.

Object reconstruction efficiencies, resolutions and fake rates are assumed to be similar in the Run-2 and HL-LHC environments, based on the assumption that the planned upgrades of the ATLAS and CMS detectors will compensate for the effects of the increase of instantaneous luminosity and higher pile-up environment at HL-LHC. For the systematic uncertainties which include experimental, signal and background components, two scenarios have been considered. The first scenario (S1) assumes the same values as those used in the published Run-2 analyses. The second scenario (S2) implements a reduction of the systematic uncertainties according to the improvements expected to be reached at the end of HL-LHC program in twenty years from now: the correction factors follow the recommendations from Ref. [119]. In certain analyses some of the systematic uncertainties are treated in a specific way, and this is discussed explicitly in each corresponding section. In all analyses, the theory uncertainties for signal and background are generally halved, except where more precise extrapolated values have been provided. Details on the projections of theoretical uncertainties are given in Section 2.2.2. The reduction of the theory uncertainties in gluon-fusion Higgs production is for instance associated to a better understanding of the correlation of their components, leading to their sum in quadrature in scenario S2, instead of the linear sum used in S1 (see Section 2.2.2.1 for details). The uncertainties related to missing higher orders in theory calculations are in particular discussed in Section 2.2.5: these uncertainties are halved in all analyses extrapolation in scenario S2, even though larger improvements are expected in some cases (e.g. gluon-fusion Higgs production). The uncertainty on the luminosity is set to 1%. The uncertainty related to Monte Carlo samples statistics is assumed to be negligible.

The extrapolated results are generally limited by systematic uncertainties. It is worth noting that, despite all efforts to design proper projections, the values of the systematic uncertainties of the Run-

[7] Contacts: M. Delmastro, N. De Filippis, P. Francavilla, A. Gilbert, S. Jezequel, P. Milenovic, M. Testa

2 analyses cannot fully account neither for the HL-LHC data-taking conditions, nor for the level of understanding of the various sources of systematic uncertainties that will be achieved by fully exploiting the large HL-LHC statistic. The systematic models in current Run-2 analyses are in fact designed for the needs of Run-2, and hence lack flexibility and details needed to account for full-fledged HL-LHC analyses. In this sense, these extrapolated uncertainties are to be considered an approximation: future analyses will exploit and gain sensitivity from phase space regions that are not accessible yet, or use analysis techniques that reduce the impact of systematic uncertainties. In many cases one can as well expect that several uncertainties will be be highly constrained with very large luminosity, and therefor updated uncertainty models with greater flexibility will be needed to properly fit the data.

In the following, all analyses segment the selected events according to the objects produced in association with the Higgs boson decay products and their topology, in order to maximise the sensitivity to the main Higgs production modes ($gg\mathrm{F}+b\bar{b}H$, VBF, $VH = qqZH+ggZH+WH$ and top = $t\bar{t}H+tH$) and to reduce the uncertainties on the respective cross sections. Details on how this segmentation is performed, and on the event selection and categorisation in the various analyses, are found in the Run-2 analysis references quoted in each section.

2.3.2 $H \to \gamma\gamma$[8]

The measurement of the Higgs boson properties in the $H \to \gamma\gamma$ channel is performed using the events that contain two isolated photon candidates passing good quality requirements in the precision regions of the detectors. Events are further segmented according to the objects accompanying the di-photon system, in order to maximise the sensitivity to the main Higgs production modes and to reduce the uncertainties on the respective cross sections, as well as to the Simplified Template Cross Section (STXS, first introduced in Refs. [45, 120]) in the merged version of Stage-1. The Higgs production cross sections are measured for a Higgs boson absolute rapidity $|y_H|$ smaller than 2.5, and with further requirements on the objects accompanying the di-photon system (e.g. jet p_{T}). The $H \to \gamma\gamma$ signal is extracted by means of a combined signal-plus-background fit of the di-photon invariant mass spectra in the various event categories, where both the continuous background and the signal resonance are parametrised by analytic functions. The shape properties of the signal PDF are obtained by Monte Carlo (MC) simulation, and constrained by performance studies of the photon energy scale and resolution. The background PDF is completely determined by the fit on data, with systematic uncertainties attributed to the specific choice of functional form following the procedure described in Ref. [11] or using the discrete profiling method [121]. More details on the analyses methods can be found in most recent measurements in the $H \to \gamma\gamma$ channel published by ATLAS [122] and CMS [123].

The performance of the measurement of the Higgs boson properties in the $H \to \gamma\gamma$ channel at HL-LHC is extrapolated from the most recent measurements by ATLAS with $80\,\mathrm{fb}^{-1}$ [122] and by CMS with $36\,\mathrm{fb}^{-1}$ [123]. The main systematic uncertainties affecting the results are the background modelling uncertainty, missing higher order uncertainties causing event migrations between the bins, photon isolation efficiencies and jet uncertainties. On top of the common assumptions mentioned in Section 2.3.1, the results of the studies performed by ATLAS include a 10% increase of the background modelling systematic uncertainties, to account for the potentially worst knowledge of the background composition in each analysis category at HL-LHC: this assumption has anyway negligible impact. In the Run-2 analyses, a conservative 100% uncertainty on the heavy flavour resonant background in top-sensitive categories is applied. Measurements by ATLAS and CMS of the heavy flavour content, or the b-jet multiplicity, are expected to better constrain these contributions: for the S2 scenario extrapolation, this uncertainty is therefore halved.

Figure 9 shows the ratio of the extrapolated $H \to \gamma\gamma$ ATLAS measurements of the cross sections times branching fraction of the main Higgs production modes to their respective theoretical SM predic-

[8] Contact: S. Falke

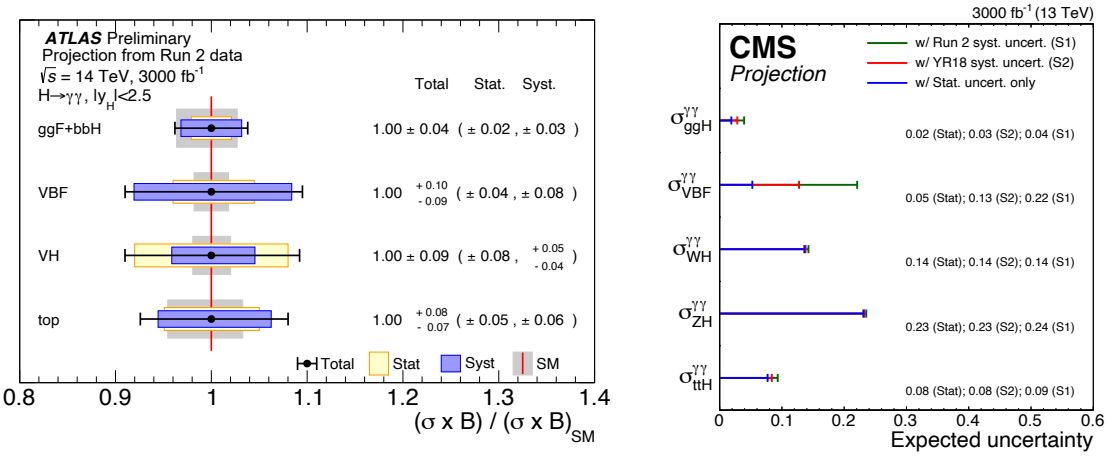

Fig. 9: Cross-section times branching fraction measurements of the main Higgs production modes in the $H \to \gamma\gamma$ decay channel, as extrapolated at the HL-LHC. In case of ATLAS results (left) the ratios of cross sections to their respective theoretical SM predictions are shown for scenario S2, while in case of CMS results (right) the uncertainties on these measurements are shown for S1, S2, and Stat-only scenarios..

tions (left), and uncertainties on these measurements for S1, S2, and stat-only scenarios as extrapolated using the $H \to \gamma\gamma$ CMS measurements (right). CMS extrapolation is obtained from the simultaneous fit in all production and decay modes, as described in Section 2.6.1. The reduction of the total uncertainty with respect to the $80\,\mathrm{fb}^{-1}$ results ranges from a factor of about 2 (3) for the S1 (S2) scenario for the $ggH + b\bar{b}H$, VBF, top cross sections, to a factor of about 5(6) for the VH cross section, that remains dominated by the statistical uncertainty.

2.3.3 $H \to Z\gamma \to \ell\ell\gamma$[9]

Due to the small branching fraction in the SM, the $H \to Z\gamma$ decay has not yet been observed at the LHC. The experimental observed limits at the 95% confidence level are currently 6.6 times the SM prediction for a Higgs boson mass of 125.09 GeV by ATLAS and 3.9 times the SM prediction for a Higgs boson mass of 125 GeV by CMS, based on the analyses of $36\,\mathrm{fb}^{-1}$ of pp collision at $\sqrt{s} = 13$ TeV described in Ref. [124, 125].

The analyses select events with an isolated photon candidate passing good quality requirements in the precision regions of the detectors, and a di-lepton system with properties compatible with that of the decay of a Z boson. Events are separated according to lepton flavour, the event kinematic properties, and the presence of jets compatible with the VBF production of the Higgs boson, in order to maximise the signal sensitivity. The signal is sought for by means of a combined signal-plus-background fit of the photon-di-lepton invariant mass spectra in various event categories, where both the continuous background and the signal resonance are parametrised by analytic functions. The Run-2 analyses are strongly driven by statistical uncertainty, and the main systematic uncertainties are from the bias associated to the background modelling, based on the MC simulation of some background processes, and on low-statistics data control regions for others.

The extrapolations to HL-LHC are performed with a simple scaling approach, assuming the same signal and background modelling used in the Run-2 analyses. All experimental and systematic uncertainties are considered to remain the same (S1), except the uncertainty associated to the background modelling, which is taken to be negligible. The latter assumption is based on the idea that, thanks to

[9] Contact: Y. Huang

the large HL-LHC statistics and the use of modern functional modelling techniques, the background shape could be constrained exclusively using data with great accuracy, thus dramatically reducing the modelling uncertainty.

The ATLAS expected significance to the SM Higgs boson decaying in $Z\gamma$ is 4.9 σ with 3000 fb^{-1}. Assuming the SM Higgs production cross section and decay branching ratios, the signal strength is expected to be measured with a ± 0.24 uncertainty. The cross section times branching ratio for the $pp \to H \to Z\gamma$ process is projected to be measured as 1.00 ± 0.23 times the SM prediction. Even at the HL-LHC scenario S1, the analysis sensitivity to $H \to Z\gamma$ will remain driven by the statistical uncertainty. The dominant source of systematic uncertainty in the extrapolation is that associated to the missing higher order uncertainties [126].

2.3.4 $H \to ZZ^* \to 4\ell$[10]

The measurement of the Higgs boson properties in the $H \to ZZ^* \to 4\ell$ channel is performed using the events that contain at least two same-flavour opposite-sign di-lepton pairs, chosen from isolated electrons and muons candidates passing good quality requirements in the precision regions of the detectors. Additional constraints on the kinematic properties of the lepton pair associated with the decay of the on-shell Z boson, and on the global topology of the event, helps to improve the signal to background ratio. The four-lepton invariant mass resolution is improved by correcting for the emission of final-state radiation photons by the leptons. The $H \to ZZ^* \to 4\ell$ signal is extracted from the four-lepton invariant mass spectra in the different event categories, after having evaluated the background components using simulations to constrain their shapes, and data control regions to extrapolate their normalisation in the signal regions. Signal to background sensitivity is in general enhanced using the multivariate and/or matrix-element based techniques. More details on the analyses methods can be found in most recent measurements in the $H \to ZZ^* \to 4\ell$ channel published by ATLAS [127] and CMS [128].

The performance of the measurement of the Higgs boson properties in the $H \to ZZ^* \to 4\ell$ at HL-LHC is extrapolated from the most recent measurements by ATLAS with 80 fb^{-1} [127], and by CMS with 36 fb^{-1} [128]. CMS extrapolation is obtained from the simultaneous fit in all production and decay modes, as described in Section 2.6.1. The dominant systematic uncertainties affecting the extrapolation of the ggH cross section measurement are the lepton reconstruction and identification efficiencies, and pile-up modelling uncertainties. The VBF and VH cross-sections are primarily affected by the uncertainty on the jet energy scale and resolution, and by the missing higher order uncertainties. These and the parton shower modelling primarily affects the extrapolated top cross section.

The VBF, VH and especially top measurements in the $H \to ZZ^* \to 4\ell$ decay channel remain largely dominated by statistical uncertainty when extrapolated to 3000 fb^{-1} while the $ggH + b\bar{b}H$ cross section is dominated by systematic uncertainties both in scenario S1 and S2. Figure 10 shows the ratio of the extrapolated $H \to ZZ^* \to 4\ell$ ATLAS measurements of the main Higgs boson production modes to their respective theoretical SM predictions in the scenario S2 (left), and uncertainties on these measurements for S1, S2, and stat-only scenarios as extrapolated using the $H \to ZZ^* \to 4\ell$ CMS measurements (right). The ggF and top $H \to ZZ^* \to 4\ell$ measurements at HL-LHC are expected to reach a level of precision comparable to the projected uncertainty on the corresponding theory predictions.

2.3.5 $H \to WW^* \to \ell\nu\,\ell\nu$[11]

The measurement of the Higgs boson properties in the $H \to WW^* \to e\nu\mu\nu$ channel is performed using the events that contain two opposite-charged isolated leptons passing good quality requirements in the precision region of the detectors and missing transverse momentum. Additional requirements on the event kinematic properties are applied to reduce the various background components (e.g. requirements

[10] Contacts: A. Gabrielli, A. Schaffer, V. Walbrecht
[11] Contacts: R. Gugel, K. Koeneke

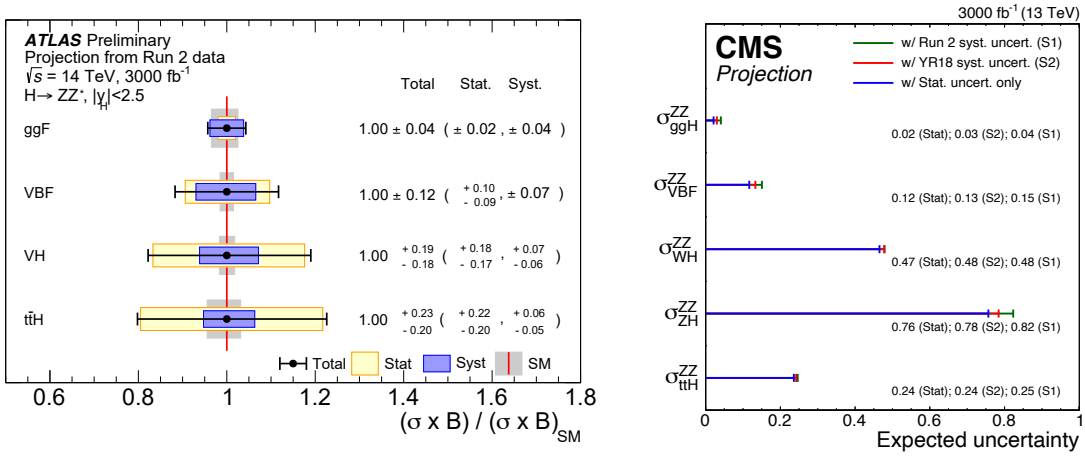

Fig. 10: Cross-section times branching fraction measurements of the main Higgs boson production modes in the $H \to ZZ^* \to 4\ell$ decay channel, as extrapolated at the HL-LHC. In case of ATLAS results (left) the ratios of cross sections to their respective theoretical SM predictions are shown for scenario S2, while in case of CMS results (right) the uncertainties on these measurements are shown for S1, S2, and Stat-only scenarios.

on the di-lepton invariant mass, transverse mass of the di-lepton + missing-transverse-energy (MET) system). Events are categorised as a function of the jet multiplicity in order to exploit the different background composition in different categories, and to help extracting the Higgs ggH and VBF production cross sections. The normalisations of the top ($t\bar{t}$ and $W+t$), and $Z \to \tau\tau$ backgrounds are set using dedicated control regions of the same jet multiplicity as the signal category to which the normalisation is transferred. In case of the (non-resonant) WW background, its normalisation is either determined using dedicated control regions (ATLAS approach) or by using theoretical prediction with corresponding uncertainty on it (CMS approach). More details on the analyses methods can be found in most recent measurements in the $H \to WW^* \to e\nu\mu\nu$ channel published by ATLAS [129] and CMS [130].

The performance of the measurements of Higgs boson properties in the $H \to WW^* \to e\nu\mu\nu$ channel at HL-LHC is extrapolated from the most recent measurements in this channel performed by ATLAS with 80 fb^{-1} [129] and by CMS with 36 fb^{-1} [130]. These measurements are completely dominated by systematic uncertainties, and their extrapolation to the S2 scenario shows the expected reduction by a factor two. The measurement of the ggH cross section by branching fraction is dominated by theoretical PDF uncertainty, followed by experimental uncertainties affecting the signal acceptance, including uncertainties on the jet energy scale and flavour composition, and lepton mis-identification; the VBF result suffers from similar dominant uncertainties. Figure 11 shows the ratio of the extrapolated $H \to WW^* \to e\nu\mu\nu$ ATLAS measurements of the main Higgs production modes to their respective theoretical SM predictions in scenario S2 (left), and uncertainties on these measurements for S1, S2, and Stat-only scenarios as extrapolated using the $H \to WW^* \to e\nu\mu\nu$ CMS measurements (right). CMS extrapolation is obtained from the simultaneous fit in all production and decay modes, as described in Section 2.6.1.

2.3.6 $H \to \tau^+\tau^-$ [12]

The measurement of the Higgs boson in the $H \to \tau^+\tau^-$ channel considers the leptonic (τ_{lep}) and the hadronic (τ_{had}) decays of the τ lepton. Three subs-channels ($\tau_{lep}\tau_{lep}$, $\tau_{lep}\tau_{had}$ and $\tau_{had}\tau_{had}$) are defined by requirements on the number of hadronically decaying τ-leptons candidates and leptons (electrons or

[12] Contacts: M. Mlynarikova, L. Thomsen

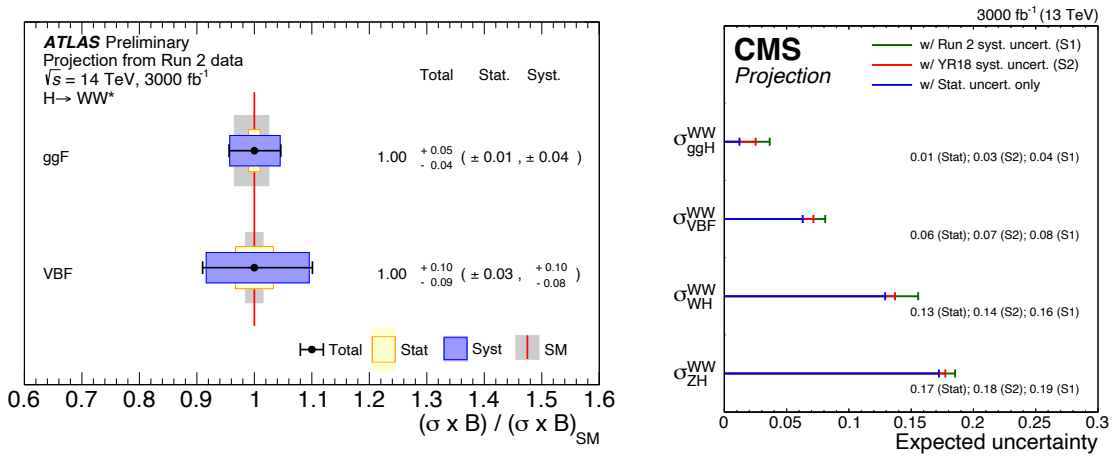

Fig. 11: Cross-section times branching fraction measurements of the main Higgs production modes in the $H \to WW^* \to e\nu\mu\nu$ decay channel, as extrapolated at the HL-LHC. In case of ATLAS results (left) the ratios of cross sections to their respective theoretical SM predictions are shown for scenario S2, while in case of CMS results (right) the uncertainties on these measurements are shown for S1, S2, and Stat-only scenarios.

muons) in the event. Candidate events are divided into categories using kinematic properties to target cases in which the Higgs boson is produced with a boost ($p_{\mathrm{T}} > 100$ GeV), primarily from gluon fusion, and cases primarily produced from vector boson fusion, in which the Higgs boson is produced with two jets separated in pseudo-rapidity. Additional requirements are employed to discriminate signal from background. One of the most important variables is the mass of the $\tau\tau$ system, calculated in ATLAS with the Missing Mass Calculator [131], and in CMS with a dynamical likelihood technique named SVFit [132]. The normalisation of the dominant backgrounds ($Z \to \ell^+\ell^-$, $t\bar{t}$, Fake-τ_{had}) is determined using dedicated control regions, or extracted directly in each signal region ($Z \to \tau^+\tau^-$, the dominant and irreducible background). More details on the analysis methods can be found in the most recent measurements in the $H \to \tau^+\tau^-$ channels published by ATLAS [133] and CMS [134].

The performance of the measurements of Higgs boson properties in the $H \to \tau^+\tau^-$ channel at HL-LHC is extrapolated from the recent measurements in this channel performed by ATLAS [135] and by CMS [134] with 36 fb^{-1}. The measurements of the cross sections for the gluon fusion and vector boson fusion production modes are dominated by systematic uncertainties, as can be seen in Table 25, which lists the total expected uncertainties on the cross sections normalised to their SM values as well as the different contributions from different types of uncertainties. The dominant contributions, the experimental and background modelling errors, are due to uncertainties on jet calibration and resolution, on the reconstruction of the E_T^{miss}, and on the determination of the background normalisation from signal and control regions.

Figure 12 shows the ratio of the extrapolated $H \to \tau^+\tau^-$ ATLAS measurements of the main Higgs production modes to their respective theoretical SM predictions in scenario S2 (left), and uncertainties on these measurements for S1, S2, and Stat-only scenarios as extrapolated using the $H \to \tau^+\tau^-$ CMS measurements (right). In case of the ATLAS extrapolation, the SM uncertainties are divided by two compared to their current values, which approximately corresponds to the scaling expected from S2 scenario. The figure shows that at the HL-LHC the measurement will reach a level of precision which is similar to the theory predictions. These systematic uncertainties are dominated by the theoretical errors on the signal acceptance for the gluon fusion measurement both for S1 and S2. In the measurement of the vector boson fusion cross section, the effects of the experimental errors and uncertainties on the background modelling become more relevant, particularly in S2.

Table 25: Expected results for the production mode cross-section measurement in the $H \to \tau^+\tau^-$ channel with 36 fb^{-1} of Run 2 data and at the HL-LHC. Uncertainties are reported relative to the SM cross section at the corresponding centre-of-mass energy. Both scenarios have been considered for the systematic uncertainties in the HL-LHC extrapolation.

Experiment, Process	ATLAS, ggF		ATLAS, VBF	
Scenario	S1	S2	S1	S2
Total uncertainty	$^{+23.1\%}_{-18.5\%}$	$^{+12.3\%}_{-10.8\%}$	$^{+9.3\%}_{-9.3\%}$	$^{+8.0\%}_{-7.6\%}$
Statistical uncert.	$^{+3.1\%}_{-3.1\%}$	$^{+3.1\%}_{-3.1\%}$	$^{+3.4\%}_{-3.4\%}$	$^{+3.4\%}_{-3.4\%}$
Experimental uncert.	$^{+6.0\%}_{-6.2\%}$	$^{+4.1\%}_{-3.9\%}$	$^{+5.2\%}_{-5.6\%}$	$^{+4.9\%}_{-4.5\%}$
Signal theory uncer.	$^{+20.3\%}_{-16.0\%}$	$^{+10.4\%}_{-9.0\%}$	$^{+6.3\%}_{-5.3\%}$	$^{+2.7\%}_{-3.3\%}$
Background theory uncer.	$^{+8.0\%}_{-5.5\%}$	$^{+3.1\%}_{-2.4\%}$	$^{+3.4\%}_{-3.4\%}$	$^{+3.8\%}_{-3.8\%}$

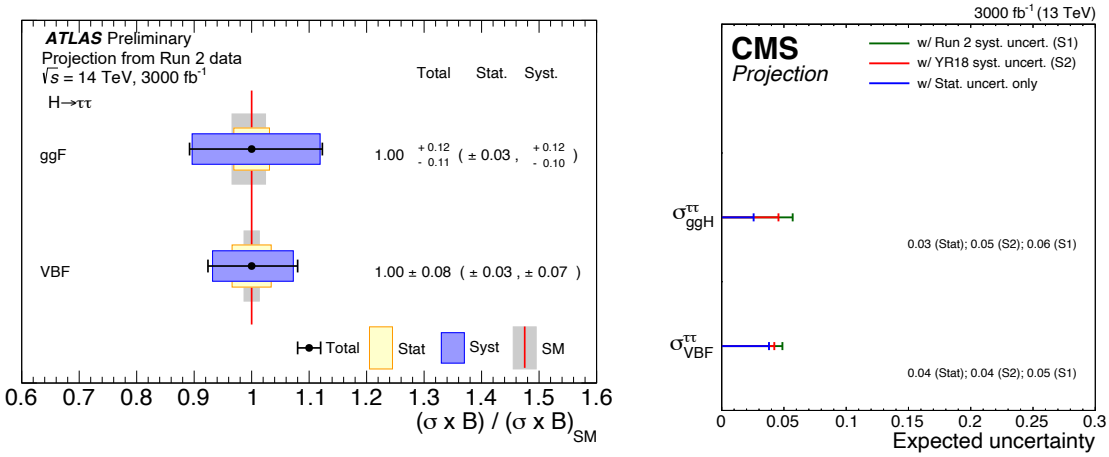

Fig. 12: (Right) ATLAS comparison, for $H \to \tau^+\tau^+$ final state applying scenario S2, between the expected precision on production-mode cross section times branching ratio normalised to their SM expectation at HL-LHC and the theoretical uncertainty on the SM prediction. (Left) CMS expected precision on production-mode cross section times branching ratio for $H \to \tau^+\tau^+$ final state in case of S1, S2, and stat-only scenarios.

2.3.7 $H \to b\bar{b}$[13]

The measurement of the Higgs boson in the $H \to b\bar{b}$ channel presented here considers the Higgs boson production in association with a vector boson ($V = W/Z$). Searches for $H \to b\bar{b}$ in association with a vector boson drove the recent observation of this decay mode reported by the ATLAS and CMS Collaborations [136, 137]. The analyses make use of leptonic decays of the vector boson for triggering and to reduce the multi-jet background: the final states of the VH system covered in the analyses always contain two b-jets and either zero, one or two electrons or muons. Both leptons are required to have the same flavour in the two lepton selection. Major backgrounds arising from SM production of vector boson plus heavy- or light-flavour jets, in addition to $t\bar{t}$ production, are controlled and constrained via dedi-

[13] Contacts: L. D'eramo, C. Li, G. Marchiori, A. de Wit

cated control regions. The b-jet energy resolution is improved by using multivariate energy regression techniques (CMS), or sequential corrections (ATLAS), and a boosted decision tree is used to improve the discrimination between signal and background. The distribution of this multivariate discriminator is used as the discriminating variable in the signal extraction fit.

The ATLAS and CMS Collaborations have both recently reported the observation of the $H \to b\bar{b}$ decay [136, 137]. The studies presented here are performed by extrapolating this most recent ATLAS $H \to b\bar{b}$ measurements using a dataset corresponding to an integrated luminosity of 78.9 fb^{-1}, and by extrapolating a previous analysis by the CMS Collaboration. In this previous analysis evidence for the $H \to b\bar{b}$ decay in the VH production mode was reported using a dataset corresponding to an integrated luminosity of 35.9 fb^{-1} [138].

Figure 13 shows the extrapolation of the signal strength uncertainty per-channel (CMS) and per-production mode (ATLAS). The details of the contributions of different sources of uncertainty in scenarios S1 and S2 for the projection of the ATLAS and CMS analyses are shown in Table 26. The large improvement, by a factor 2.5–3, in the uncertainty of the measurement for the WH (1-lepton channel) compared to the Run-2 results (around 45%) is caused by the integrated luminosity scaling of the uncertainty in the modelling of the W boson p_{T} distribution for both the collaborations, being the dominant uncertainty in scenario S1.

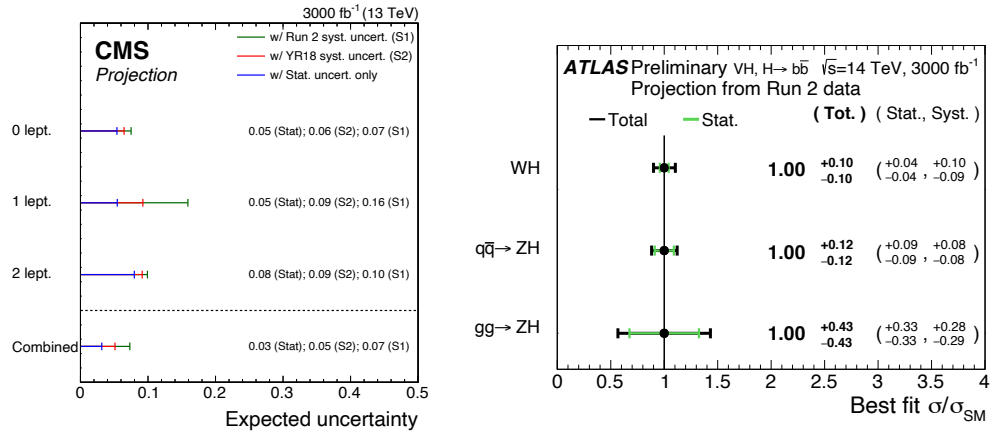

Fig. 13: Extrapolation of the uncertainties estimated by the CMS collaboration (left) and by the ATLAS collaboration (right) for the $H \to b\bar{b}$ channel. The figure gives the uncertainties per-channel and on the combined signal strengths on the left, and per-production mode on the right. Values are given for the S1 (with Run 2 systematic uncertainties [138]) and S2 (with YR18 systematic uncertainties) scenarios, as well as a scenario in which all systematic uncertainties are removed. Only the S2 scenario is presented in the plot by the ATLAS collaboration (S1 is presented in Table 26).

Both in scenario S1 and S2 the largest component of the systematic uncertainty is theoretical. This arises from the uncertainty in the gluon-induced ZH ($gg \to ZH$) production cross section due to QCD scale variations. The $gg \to ZH$ process contributes a small fraction of the total ZH process. Despite this, the uncertainty in the production cross section for this process due to QCD scale variations becomes dominant because it is very large: 25% for the $gg \to ZH$ process, compared to approximately 0.7% for the $qq \to ZH$ process [45]. The theoretical uncertainties on the $gg \to ZH$ production are reduced to 15% in the S2. An important contribution to the uncertainty is due to category-acceptance uncertainties in the dominant $Z+b\bar{b}$ and $W+b\bar{b}$ backgrounds due to QCD scale variations, as well as the uncertainty in the $qq \to ZH$ and WH production cross section due to QCD scale variations. To improve the precision of the measurement it is therefore important to improve these theoretical uncertainties.

Table 26: Contributions of particular groups of uncertainties, expressed as percentages, in S1 (with Run 2 systematic uncertainties [138]) and S2 (with YR18 systematic uncertainties) for the CMS and ATLAS analyses of the $H \to b\bar{b}$ channel. The total uncertainty is decomposed into four components: signal theory, background theory, experimental and statistical. In the CMS results, the signal theory uncertainty is further split into inclusive and acceptance parts, and the contributions of the b-tagging and JES/JER uncertainties to the experimental component are also given. In the ATLAS results, the contributions of the four groups of uncertainties are presented for $pp \to WH$, $qq \to ZH$ and $gg \to ZH$ separately.

Experiment	CMS	
Process	$pp \to VH$	
Scenario	S1	S2
Total uncertainty	7.3%	5.1%
Statistical uncert.	3.2%	3.2%
Experimental uncert.	2.6%	2.2%
b-tagging	2.2%	2.0%
JES and JER	0.7%	0.6%
Signal theory uncer.	5.4%	2.6%
Inclusive	4.6%	2.2%
Acceptance	2.7%	1.3%
Background uncert.	2.8%	2.3%

Experiment	ATLAS					
Process	$pp \to WH$		$qq \to ZH$		$gg \to ZH$	
Scenario	S1	S2	S1	S2	S1	S2
Total uncertainty	$^{+14.9\%}_{-13.8\%}$	$^{+10.4\%}_{-10.0\%}$	$^{+13.8\%}_{-13.2\%}$	$^{+12.1\%}_{-11.8\%}$	$^{+49.8\%}_{-49.0\%}$	$^{+43.2\%}_{-43.3\%}$
Statistical uncert.	$^{+4.1\%}_{-4.1\%}$	$^{+4.1\%}_{-4.1\%}$	$^{+9.0\%}_{-8.9\%}$	$^{+9.0\%}_{-8.9\%}$	$^{+33.3\%}_{-33.3\%}$	$^{+33.3\%}_{-33.3\%}$
Experimental uncert.	$^{+4.8\%}_{-4.7\%}$	$^{+4.4\%}_{-4.3\%}$	$^{+6.5\%}_{-6.3\%}$	$^{+5.7\%}_{-5.5\%}$	$^{+24.9\%}_{-25.0\%}$	$^{+20.8\%}_{-20.4\%}$
Signal theory uncer.	$^{+8.0\%}_{-7.0\%}$	$^{+4.6\%}_{-4.1\%}$	$^{+6.1\%}_{-5.5\%}$	$^{+3.1\%}_{-2.8\%}$	$^{+18.1\%}_{-14.0\%}$	$^{+9.6\%}_{-8.0\%}$
Background uncert.	$^{+10.8\%}_{-10.0\%}$	$^{+7.2\%}_{-6.9\%}$	$^{+5.4\%}_{-4.8\%}$	$^{+4.8\%}_{-4.6\%}$	$^{+20.7\%}_{-21.8\%}$	$^{+17.7\%}_{-18.1\%}$

In the future, and at the HL-LHC in particular, the b-tagging efficiency may change. The conditions could worsen the efficiency, but at the same time new detectors and new techniques could also lead to an improvement in the b-tagging efficiency. The effect of changes in b-tagging efficiency on the overall signal strength uncertainty has been evaluated by the CMS collaboration, showing that an improvement of 10% in the b-tagging efficiency leads to a relative improvement in the signal strength uncertainty of up to 6% [139].

2.3.8 $H \to \mu^+\mu^-$[14]

The $H \to \mu^+\mu^-$ analyses play a crucial role in the determination of the couplings to the second fermion generation. The analyses search for a narrow peak in the di-muon invariant mass over a smoothly falling background, dominated by Drell–Yan and top-pair productions. Events are selected requiring two op-

[14] Contacts: M. Klute, H. Li, G. Marchiori, A.Marini, M. Verducci, M. Zgubic, J. Zhang

positely charged muons passing loose quality criteria to retain as much signal as possible. The overall sensitivity to this decay mode benefits from multivariate or sequential categorisation techniques that allow separating the two dominant production modes, the vector boson fusion (with the typical presence of a forward-backward jet pair) and the gluon fusion. Additional enhancements in the sensitivity are achieved by a further sub-categorisation based on the muon momentum resolution. More details on the analysis methods can be found in the most recent searches of the $H \to \mu^+\mu^-$ channels published by ATLAS [140] and CMS [141].

The extrapolation studies presented here by ATLAS Collaboration are based on a previous analysis performed by that collaboration using the 2015–2017 proton-proton collision dataset collected at $\sqrt{s} = 13\,\text{TeV}$, which corresponds to an integrated luminosity of $79.8\,\text{fb}^{-1}$ [140]. In addition to the standard extrapolation procedure, the di-muon signal widths are reduced by 15-30% thanks to the improvements expected from the performance of the ATLAS upgrade Inner Tracker (ITk) [20]. In this analysis, the $Z \to \mu^+\mu^-$ background is fully determined by data, and it is modelled by fitting the di-muon invariant mass $m_{\mu\mu}$ distribution in each category using a Breit–Wigner function convoluted with a Gaussian summed to a smooth function.

Similar studies have been carried out by the CMS Collaboration, based on the analysed data collected during 2016 and corresponding to an integrated luminosity of $36\,\text{fb}^{-1}$ [142]. The analysis was optimised to have the overall best sensitivity to a standard model Higgs boson inclusively with respect to the production modes with the data collected in 2016. In addition to the extrapolation procedure based on the increased luminosity, the di-muon invariant mass width is reduced in order to match the expected increase in performances due to the upgrade in the tracking system [22] and displayed in Fig. 14. The di-muon mass resolution plays a crucial role in the analysis performances and in the systematic uncertainty induced by the choice of the background function. The CMS experiment [143] benefits from the large $4\,\text{T}$ solenoidal fields that allowed it to achieve down to 1.1% di-muon mass resolution in 2016 and, with the upgrade projects, the CMS detector will be able to reach in the best category a di-muon mass resolution of 0.65% [22].

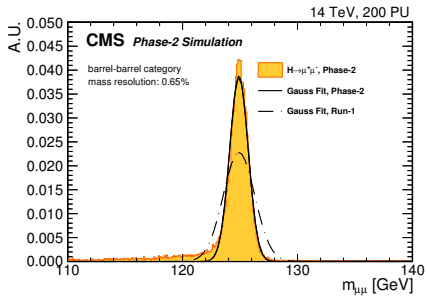

Fig. 14: The di-muon invariant mass distribution for $H \to \mu^+\mu^-$ decays for muons in the central region, simulated with the Phase-2 detector. [22].

Table 27 shows the expected precision on the signal strength (ATLAS) and branching fraction (CMS) measurement with $3000\,\text{fb}^{-1}$ of HL-LHC data in the scenarios S1 and S2. In both scenarios, the analysis is limited by the statistical uncertainty, while the leading systematic uncertainty is the bias introduced by the choice of the function describing the background (spurious signal uncertainty), and the uncertainties on the modelling of the signal (their reduction in S2 contributes to an overall improvement of 10% on the precision of the measurement). Expected uncertainties on signal strength vary from 15 to 13% (ATLAS) and on the branching fraction vary from 13 to 10% (CMS), accordingly to the projection scenario. CMS extrapolation is obtained from the simultaneous fit in all production and decay modes, as described in Section 2.6.1.

Table 27: Expected precision on the signal strength measurement in the $H \to \mu^+\mu^-$ channels with 3000 fb^{-1} of HL-LHC data with the two systematic uncertainties scenarios. For the HL-LHC extrapolation, the improved ITk resolution has been emulated.

Experiment	ATLAS	
Process	Combination	
Scenario	S1	S2
Total uncertainty	$^{+15\%}_{-14\%}$	$^{+13\%}_{-13\%}$
Statistical uncert.	$^{+12\%}_{-13\%}$	$^{+12\%}_{-13\%}$
Experimental uncert.	$^{+3\%}_{-3\%}$	$^{+2\%}_{-2\%}$
Theory uncer.	$^{+8\%}_{-5\%}$	$^{+5\%}_{-4\%}$

Experiment	CMS	
Process	Combination	
Scenario	S1	S2
Total uncertainty	13%	10%
Statistical uncert.	9%	9%
Experimental uncert.	8%	2%
Theory uncer.	5%	3%

2.4 Fiducial and differential cross-section measurements[15]

2.4.1 Measurements using $H \to \gamma\gamma$, $H \to ZZ^* \to 4\ell$, (boosted) $H \to b\bar{b}$ decay channels[16]

In the context of Higgs boson property measurements, one of the main goals of HL-LHC, differential measurements provide a probe of various Higgs boson properties by looking at distortions of differential distributions. The $p_{\mathrm{T}}^{\mathrm{H}}$ distribution is of particular interest, as potential new physics may reside in the tails of the distribution, which cannot be measured in inclusive measurements [144, 145, 146]. Differential Higgs boson production cross section measurements are available for a range of observables from both the ATLAS [147, 148, 149, 150, 151, 152] and CMS [153, 154, 155, 156, 128, 157] Collaborations at $\sqrt{s}$ = 8 and 13 TeV.

The most recent $p_{\mathrm{T}}^{\mathrm{H}}$ spectra at $\sqrt{s}$ = 13 TeV from both the ATLAS [152] and CMS [157] Collaborations are projected to an integrated luminosity of 3000 fb^{-1} [139, 158]. The projection of the $p_{\mathrm{T}}^{\mathrm{H}}$ differential cross section measurement by the CMS Collaboration is shown in Fig. 15, for both scenarios S1 and S2. The corresponding total uncertainties are respectively given in Tables 28 and 29. With respect to the uncertainties affecting the measurement based on an integrated luminosity of 35.9 fb^{-1}, the uncertainties at 3000 fb^{-1} in the higher $p_{\mathrm{T}}^{\mathrm{H}}$ region are about a factor of ten smaller. This is expected, as the uncertainties in this region remain statistically dominated. The uncertainties in the lower $p_{\mathrm{T}}^{\mathrm{H}}$ region are however no longer statistically dominated, as can been seen by comparing Table 28 with Table 29,

[15] Contacts: M. Delmastro, A. Gilbert, T. Klijnsma, J. Langford, W. Leight, R. Naranjo Garcia, A. Salvucci, M. Scodeggio, K. Tackmann, N. Wardle, C. Vernieri

[16] Contacts: M. Delmastro, T. Klijnsma

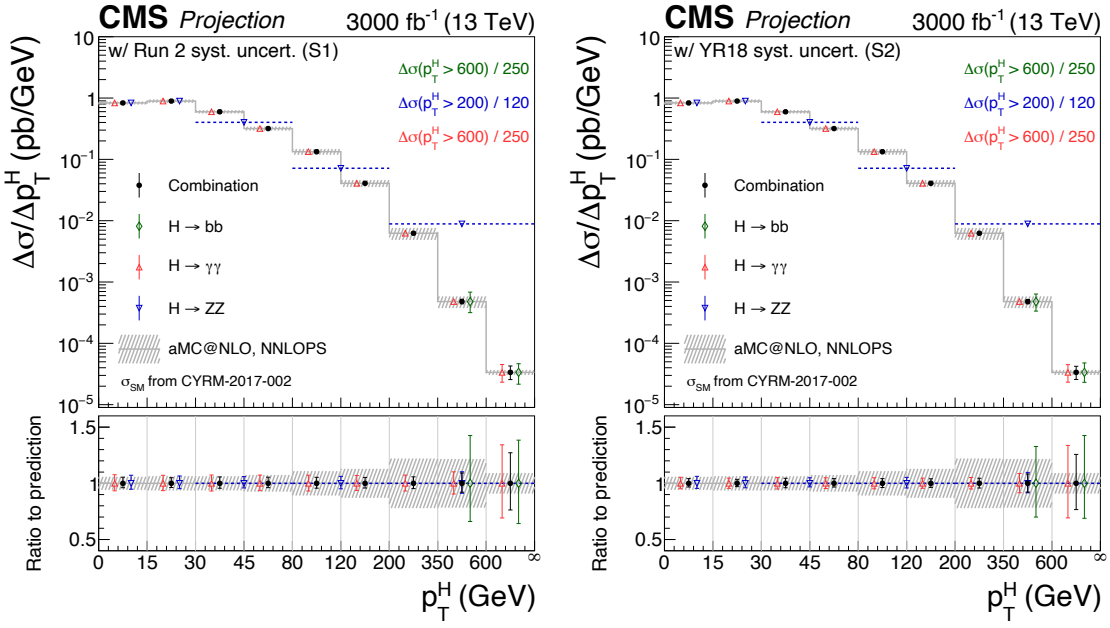

Fig. 15: Projected differential cross section for $p_{\mathrm{T}}{}^{\mathrm{H}}$ at an integrated luminosity of 3000 fb^{-1} [157], under S1 (upper, with Run 2 systematic uncertainties [159]) and S2 (lower, with YR18 systematic uncertainties).

where the reduced systematic uncertainties in S2 yield a reduction in the total uncertainty of up to 25% compared to S1.

Figure 16 shows the ATLAS projections to 3000 fb^{-1} of the differential measurements of $p_{\mathrm{T}}{}^{\mathrm{H}}$, the Higgs rapidity $|y_H|$, the jet multiplicity N_{jets} of jets with $p_{\mathrm{T}} > 30$ GeV and the transverse momentum of the leading jet accompanying the Higgs boson p_{H}^{j1}, as obtained by combining the measurement in the $H \to \gamma\gamma$ and $H \to ZZ^* \to 4\ell$ channels, in scenarios S1 and S2. The relative uncertainties affecting the $p_{\mathrm{T}}{}^{\mathrm{H}}$ measurement are given in Tables 28 and 29. The ATLAS combined $p_{\mathrm{T}}{}^{\mathrm{H}}$ measurement extrapolation exhibits relative uncertainties ranging from about 5% in the lower $p_{\mathrm{T}}{}^{\mathrm{H}}$ bins to about 9% in the highest $p_{\mathrm{T}}{}^{\mathrm{H}}$ bin in scenario S1, reducing to uncertainties ranging from $\sim 4\%$ to $\sim 8\%$ in scenario S2.

Due to a different choice of $p_{\mathrm{T}}{}^{\mathrm{H}}$ binning by ATLAS and CMS, and the lack of a more sophisticated study of the correlation of systematic uncertainties, it was chosen not to combine the projected spectra presented above. Instead, the projections from CMS are scaled to an integrated luminosity of 6000 fb^{-1}, providing a proxy estimate of the overall sensitivity of an eventual combination of measurements by the two experiments. Figure 17 shows the CMS projection at 6000 fb^{-1}, with the same systematic scaling as for the projection at 3000 fb^{-1}. As expected at very high integrated luminosity, the systematic uncertainties dominate the statistical ones.

2.4.2 *Measurement of $p_T(H)$ spectrum in $t\bar{t}H$ production mode*[17]

This section describes the strategy for measuring the differential p_T cross section for Higgs boson production in association with at least one top quark, and decaying to photons ($\mathrm{t\bar{t}H} + \mathrm{tH}$, $\mathrm{H} \to \gamma\gamma$), at the High-Luminosity LHC with the CMS Phase-2 detector. The $\mathrm{H} \to \gamma\gamma$ decay mode provides a final state in which the decay of the Higgs boson can be fully reconstructed, and a direct measurement of the p_T differential cross-section can be made.

[17] Contacts: N. Wardle, J. Langford

Table 28: Relative uncertainties on the projected $p_{\mathrm{T}}^{\mathrm{H}}$ spectrum measurements by ATLAS and CMS under S1 at 3000 fb^{-1}. The relative uncertainty of the CMS projection is also given at 6000 fb^{-1} to represent the sensitivity achievable by an eventual ATLAS and CMS combination.

3000 fb^{-1} ATLAS											
$p_{\mathrm{T}}^{\mathrm{H}}$ [GeV]	0-10	10-15	15-20	20-30	30-45	45-60	60-80	80-120	120-200	200-350	350-1000
H $\to \gamma\gamma$	6.5%	5.9%		6.2%	6.0%	6.5%	6.7%	6.0%	5.4%	6.3%	9.5%
H $\to$ ZZ	9.0%	8.1%	8.9%	6.9%	6.3%	6.8%	6.8%	6.2%	6.7%	13.2%	24.3
Combination	5.5%	4.8%		5.0%	4.7%	5.0%	5.1%	4.6%	4.4%	5.4%	8.7%

3000 fb^{-1} CMS									
$p_{\mathrm{T}}^{\mathrm{H}}$ [GeV]	0-15	15-30	30-45	45-80	80-120	120-200	200-350	350-600	600-∞
H $\to \gamma\gamma$	5.1%	6.8%	7.1%	6.9%	7.1%	6.7%	7.1%	9.9%	32.5%
H $\to$ ZZ	5.4%	5.7%	5.0%		5.5%		9.6%		
H $\to$ bb	none							38.2%	37.1%
Combination	4.7%	4.4%	5.0%	4.7%	4.8%	4.7%	5.2%	8.5%	25.4%

6000 fb^{-1}									
Combination	4.0%	3.7%	4.0%	3.9%	4.0%	4.0%	4.3%	6.3%	18.3%

Table 29: Relative uncertainties on the projected $p_{\mathrm{T}}^{\mathrm{H}}$ spectrum measurements by ATLAS and CMS under S2 at 3000 fb^{-1}. The relative uncertainty of the CMS projection is also given at 6000 fb^{-1} to represent the sensitivity achievable by an eventual ATLAS and CMS combination.

3000 fb^{-1} ATLAS											
$p_{\mathrm{T}}^{\mathrm{H}}$ [GeV]	0-10	10-15	15-20	20-30	30-45	45-60	60-80	80-120	120-200	200-350	350-1000
H $\to \gamma\gamma$	5.3%	4.6%		4.9%	4.7%	5.4%	5.7%	4.9%	4.2%	5.1%	8.7%
H $\to$ ZZ	8.3%	7.6%	8.3%	6.3%	5.7%	6.2%	6.3%	5.7%	6.4%	13.1%	23.2%
Combination	4.5%	3.8%		3.9%	3.6%	4.1%	4.2%	3.7%	3.5%	4.5%	8.2%

3000 fb^{-1} CMS									
$p_{\mathrm{T}}^{\mathrm{H}}$ [GeV]	0-15	15-30	30-45	45-80	80-120	120-200	200-350	350-600	600-∞
H $\to \gamma\gamma$	5.1%	4.6%	5.1%	4.8%	4.9%	4.5%	5.1%	8.6%	32.2%
H $\to$ ZZ	5.4%	4.8%	4.1%		4.7%		9.1%		
H $\to$ bb	none							31.4%	36.8%
Combination	3.7%	3.3%	4.2%	3.7%	4.0%	3.8%	4.4%	8.0%	24.5%

6000 fb^{-1}									
Combination	2.9%	2.6%	3.2%	2.9%	3.0%	2.9%	3.2%	5.8%	17.9%

The expected precision of the analysis is determined based on simulated proton-proton (pp) events, at a centre of mass energy of 14 TeV. Simulated signal and background events are generated using a combination of POWHEG v2.0 [160, 81], MADGRAPH5_AMC@NLO v2.2.2 [79], SHERPA v2.2.5 [161], and interfaced with PYTHIA v8.205 [32]. The signal and background events are processed with DELPHES [13], using the CMS Phase-2 card, to simulate the response of the upgraded CMS detector to showered particles. Full details of the analysis can be found in Ref. [162].

2.4.2.1 Analysis strategy

An event selection is applied to the simulated background and signal events following a similar strategy to the CMS Run 2 H $\to \gamma\gamma$ strategy [123]. The events are required to contain two photons, with $|\eta^{\gamma}| < 2.4$ excluding the region $1.44 < |\eta^{\gamma}| < 1.57$, with an invariant mass satisfying $100 < m_{\gamma\gamma} < 180$ GeV, where the leading-p_T (sub-leading-p_T) photon satisfies $\mathrm{p}_T^{\gamma}/m_{\gamma\gamma} > 1/3$ (1/4). The two photons are also required to be separated by $\Delta R_{\gamma\gamma} > 0.4$. The photons must also be isolated, which is achieved by requiring that the sum of charged transverse momentum in a cone of radius $\Delta R_{\gamma} = 0.4$, centred on the photon direction, is less than $0.3\,\mathrm{p}_T^{\gamma}$. For events where more than one photon pair passes the selection, then the pair with $m_{\gamma\gamma}$ closest to the Higgs boson mass is chosen.

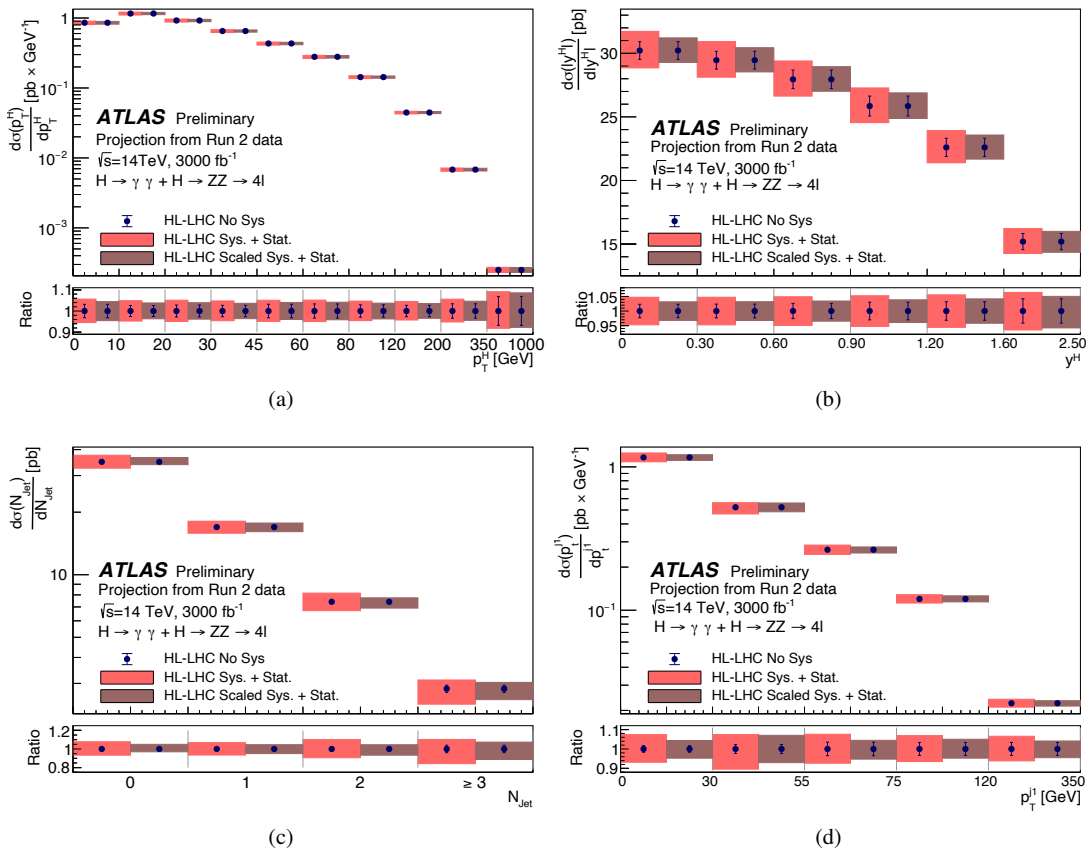

Fig. 16: Differential cross sections measured by ATLAS in the full phase space, extrapolated to the full HL-LHC luminosity for the combination of the $H \to \gamma\gamma$ and $H \to ZZ^* \to 4\ell$ decay channels for (a) Higgs boson transverse momentum $p_{\mathrm{T}}{}^{\mathrm{H}}$, (b) Higgs boson rapidity $|y_H|$, (c) number of jets N_{jets} with $p_{\mathrm{T}} > 30$ GeV, and (d) the transverse momentum of the leading p_{H}^{j1}. For each point both the statistical (error bar) and total (shaded area) uncertainties are shown. Two scenarios are shown: one with the current Run2 systematic uncertainty (S1) and one with scaled systematic uncertainties (S2).

In order to isolate the production of the Higgs boson in association with top quarks, the selection requires all events to have at least one $b-$tagged jet. Such events are separated into two orthogonal categories based on the decay products of the top quark, a hadronic category and a leptonic category. In the hadronic category, events must contain at least 3 jets, clustered using the anti-k_T algorithm with a cone size of 0.4, separated by $\Delta R > 0.4$ with respect to both photon candidates. The jets are required to have $\mathrm{p}_T > 25$ GeV and $|\eta| < 4$. In the leptonic category, only 2 jets are required, however, in addition, the events must contain at least one isolated muon or electron. The muons or electrons must satisfy $\mathrm{p}_T > 20$ GeV and $|\eta| < 2.4$, excluding the region $1.44 < |\eta^{\gamma}| < 1.57$ for electrons. The muons must satisfy an isolation requirement that the sum of all reconstructed particles p_T, inside a cone of radius $\Delta R = 0.4$, excluding the muon itself, is less than 0.25 times the transverse momentum of the muon. In addition, for electrons, the invariant mass of pairs formed from the electron and either selected photon, $m_{e\gamma}$, is required to be greater than 95 GeV to reduce contamination from $Z \to e^+e^-$ decays. Events passing the leptonic category selection are excluded from the hadronic selection to maintain orthogonality of the two categories. For the signal extraction, boosted decision tree (BDT) classifiers are trained independently in each channel, which distinguish between signal-like and background-like events, using input variables related to the kinematics of the events, such as the lepton and jet momenta

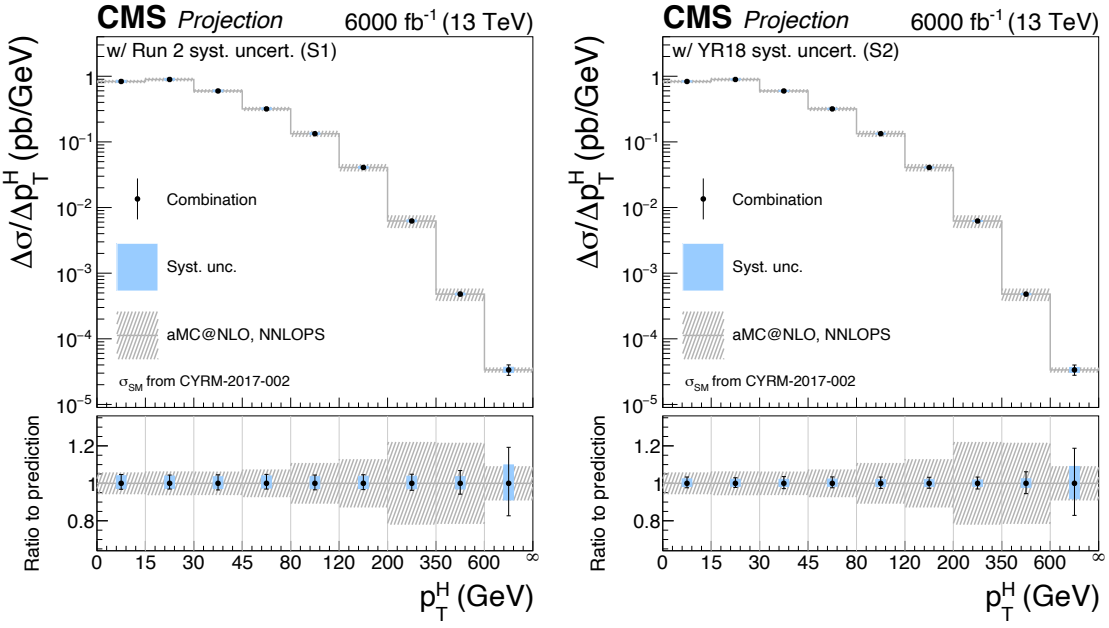

Fig. 17: Projected differential cross section for $p_{\mathrm{T}}{}^{\mathrm{H}}$ at an integrated luminosity of 6000 fb^{-1} (representing the sensitivity achievable by an eventual ATLAS and CMS combination), under scenarios S1 and S2.

and pseudo-rapidities, and the scalar sum of transverse momentum of all final state objects in the event. Events are required to have output BDT values greater than fixed thresholds, which are tuned to provide the best sensitivity to κ_λ. The hadronic category is further split into two different regions of BDT output, for events with di-photon transverse momentum ($\mathrm{p}_T^{\gamma\gamma}$) less than 350 GeV, to reduce the contamination of gluon fusion Higgs boson production.

Finally, the events are further divided into six bins of $\mathrm{p}_T^{\gamma\gamma}$, given in Tab. 30, making a total of 17 categories.

Table 30: bin boundaries which define the $p_{\mathrm{T}}{}^{\mathrm{H}}$ regions for which the differential cross sections are measured. These also correspond to the bins in which the hadronic and leptonic event categories are sub-divided.

p_T^H or $\mathrm{p}_T^{\gamma\gamma}$ bin boundaries (GeV)						
0	45	80	120	200	350	∞

Experimental systematic uncertainties are included in the signal model, which can cause migration both between the different categories and in and out of the fiducial region. The dominant uncertainties are related to the reconstruction and identification efficiencies for photons and b jets as well as the energy scale and resolution of reconstructed jets. Furthermore, theoretical uncertainties are included on the rates of ggH and VH contamination, which modify both the overall normalisation and the relative contamination between the different categories for these processes. The background estimation follows the same strategy as in the CMS Run 2 H $\rightarrow \gamma\gamma$ analysis [123], in that the parameters of the background functions are free to float in the fit, and constrained directly from the data. Therefore the uncertainties on the background will be statistical in nature. However, the impact of increasing the rate of fake photons in the background component has been studied and was found to reduce the sensitivity to κ_λ by roughly 10% in the worst case scenario [162].

2.4.2.2 *Differential cross-section results*

In order to account for resolution effects, the signal events are separated based on the p_T^H at generator level. Signal and background models are constructed using the simulated events in each category. The signal model accounts for the relative populations of events from the different production processes as well as from different $p_T{}^H$ bins, and the di-photon mass resolution expected from events in each category. The background model is constructed from a fit of smoothly falling functions to the weighted sum of simulated background samples, accounting for the different fake photon rates for each source of background and normalised to the total background yield expected in 3000 fb$^-$1 of High-Luminosity LHC data. The differential cross-section is determined from a simultaneous maximum likelihood fit to an Asimov data set [163] corresponding to $3\,\text{ab}^{-1}$, and assuming SM Higgs boson production in each category. Systematic uncertainties are accounted for through the introduction of constrained nuisance parameters in the log-likelihood, which are profiled.

The results of this fit are given in figure 18. The results shown are unfolded back to a fiducial region which is common to both the hadronic and leptonic selections, and shown using only the hadronic or leptonic categories, and their combination. The theoretical uncertainties displayed on the predicted $t\bar{t}H + tH$ cross section are calculated by modifying the renormalisation and factorisation scales up and down by a factor of 2.

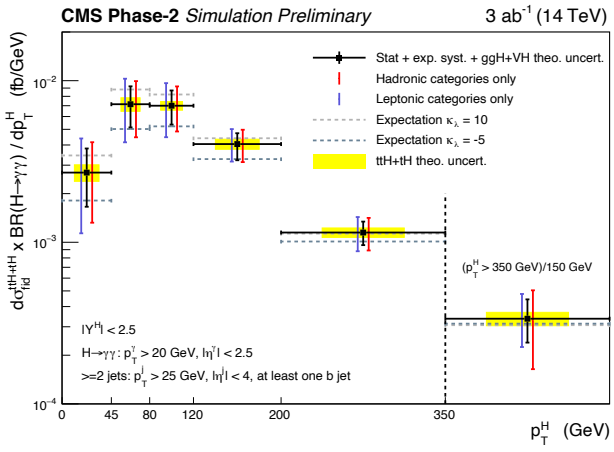

Fig. 18: The expected p_T^H differential $t\bar{t}H$ + tH cross sections times branching ratio, along with their uncertainties [162]. The error bars on the black points include the statistical uncertainty, the experimental systematic uncertainties and the theoretical uncertainties related to the ggH and VH contamination, which is subtracted in the fit. The cross section for $p_T{}^H > 350$ GeV is scaled by the width of the previous bin. The expected $t\bar{t}H$ + tH cross sections for anomalous values of the Higgs boson self-coupling (κ_λ = 10 and κ_λ = -5) are shown by the horizontal dashed lines.

2.5 Direct and indirect probing of top Yukawa coupling[18]

2.5.1 *Measurements in $t\bar{t}H$ and tH production modes*[19]

One of the main targets of the High-Luminosity LHC upgrade is to achieve precision measurements of the Higgs boson properties. The Yukawa coupling of the Higgs boson to the top quark is expected to be of the order of unity and could be partially sensitive to effects beyond the Standard Model. Therefore, a direct measurement of the coupling of the Higgs boson to top quarks is extremely important to access possible

[18] Contacts: A. Calandri, P. Das, K. El Morabit, S. Folgueras, S. Gadatsch, A. Gilbert, P. Keicher, T. Klijnsma, K. Mazumdar, M. Schröder

[19] Contacts: A. Calandri, M. Schröder